Computational Chemistry for Graphene-based Energy Applications: Progress and Challenges

Zak E. Hughes[*a] **and Tiffany R. Walsh**[a]

Received Xth XXXXXXXXXX 20XX, Accepted Xth XXXXXXXXX 20XX
First published on the web Xth XXXXXXXXXX 200X
DOI: 10.1039/b000000x

Research in graphene-based energy materials is a rapidly growing area. Many graphene-based energy applications involve interfacial processes. To enable advances in the design of these energy materials, such that their operation, economy, efficiency and durability is at least comparable with fossil-fuel based alternatives, connections between the molecular-scale structure and function of these interfaces are needed. While it is experimentally challenging to resolve this interfacial structure, molecular simulation and computational chemistry can help bridge these gaps. In this Review, we summarise recent progress in the application of computational chemistry to graphene-based materials for fuel cells, batteries and photovoltaics. We also outline both the bright prospects and emerging challenges these techniques face for application to graphene-based energy materials in future.

Introduction

Isolation of the two-dimensional allotrope of carbon known as graphene in 2004 [1] has sparked rapid growth in research of this material. Graphene possesses an abundance of desireable materials properties; high electrical and thermal conductivity, exceptional mechanical properties, high specific surface area, flexibility, corrosion resistance and optical transparency, amongst others. Many of these properties can be and have been exploited profitably in the creation of novel materials for environmentally-friendly energy conversion and energy storage solutions [2,3]. However, for these graphene-based energy storage and energy conversion materials to attain commercial viability, further advances are needed. Structural characterisation of these materials provides an essential and fundamental foundation for realising these advances.

As a complement to experimental characterisation, molecular simulation and quantum chemistry can help establish vital links between the atomic-scale structure of the graphene interfaces in these materials, and their performance in energy conversion and energy storage. Here, we review the contributions of quantum chemistry and molecular simulation to the area of graphene-based energy materials. We start with an overview of these two classes modelling approaches. Since in many of these energy applications ambient moisture will be present, we next provide a survey of progress to date in modelling and simulation of aqueous graphene interfaces. In the context of energy storage, namely batteries and supercapacitors, we next highlight the interface between electrolytes and graphene. We follow this with a comprehensive overview of the contribution, mostly from quantum chemical approaches, to developments in the field of photovoltaics and graphene-based fuel cells. We finish with a survey of progress in the area of batteries. We conclude with an outlook on the future challenges that computational chemistry faces in making further valuable qcontributions to advancing graphene-based energy materials.

Overview of Computational Methods

Over the last 60 years computational chemistry approaches and molecular simulation have emerged to become major techniques in the investigation of the physics and chemistry of materials. In this section we will provide a brief overview of background and current status of molecular simulation, for more detailed information on these topics we recommend Refs. [4,5]

Molecular simulation aims to characterise the potential energy surface (PES) of a system, in particular the location of the minima on the PES, and their connections via saddle points. The basis for such a characterisation involves two components, the *technique* used to sample the PES of the system and the *model* employed to describe the PES. The sampling technique used for a given system will depend on the nature of the system; for small system sizes, high symmetry or well-ordered systems, energy minimisation-based approaches, such as basin hopping [6,7] may be sufficient to locate the relevant basins on the PES. However, for many systems, this type of approach is not suitable, and instead the PES can only be characterised via more extensive statistical sampling of accessible basins under appropriate conditions. Traditionally there are two techniques (or more accurately classes of techniques)

[a] *Institute for Frontier Materials, Deakin University, Geelong, Australia. Fax: +61 (0)3 5227 1103; Tel: +61 (0)3 5247 9160; E-mail: tiffany.walsh@deakin.edu.au; zhughes@deakin.edu.au*

that have been used for this purpose, *Monte Carlo* (MC) and *molecular dynamics* (MD).[4,5]

In MD, the PES is sampled by taking an initial configuration and then propagating Newton's equations of motion to explore how the system will behave over time. This results in a trajectory, comprising a series of molecular configurations which, if the simulation is carried out for a suitable duration, will yield the ensemble averaged behaviour of the system. MC also relies on the accumulation of a set of configurations with the correct Boltzmann weighting. However, these configurations are generated in a different manner. In the MC approach, random changes are made to an existing configuration to generate a new configuration, this new configuration is then either accepted or rejected according to the Metropolis criterion[9]. Both techniques have advantages and disadvantages; MD provides a trajectory that is continuous in time, allowing the dynamics of the system to be investigated as well as equilibrium behaviour. MC has the advantage that only the energy, and not the derivatives of the energy, of the system needs to be calculated at each step. MC also allows the simulation of properties in the Grand Canonical (μpT) ensemble whereas MD is traditionally limited to ensembles where the number of molecules in the system remains constant. Ultimately, the nature of the system under investigation will determine which technique is the most appropriate to use. Moreover, advances in both classes of technique have overcome some of the traditional disadvantages of both classes of techniques, sometimes by blending the two, *e.g.* performing a MD simulation with occasional MC moves within it. A particular focus of molecular simulation in recent years has been the development of a series of techniques for calculating the free energy differences between two states, such methods include umbrella sampling,[10] steered MD,[11] meta-dynamics[12,13] and others.[14]

The second component of a molecular simulation is the model used to describe the interaction of all species (typically interatomic interactions) in the system. The most detailed and rigorous descriptions of molecular systems are quantum mechanical (QM) techniques, which explicitly capture the electronic degrees of freedom present in the system. There are two broad classes of QM methods, those based on Wavefunction theory (WFT), based on post-Hartree-Fock techniques, and those which make use of density functional theory (DFT). The advantage of the former methods is that they can be systematically improved; their disadvantages include their cost (making them impractical for many systems) and the fact that they are typically (but not exclusively) applied in the study of non-periodic systems. For example, a graphene sheet will be approximated by an arene ring (*e.g.* benzene or coronene, as shown in Fig 1), meaning that the delocalised states at the surface will not be captured, and edge effects may be present. The alternative QM approach, DFT, can be readily used to describe periodic systems. Unfortunately, traditional DFT functionals based on the generalised gradient approximation (GGA)[15] cannot reliably recover the dispersion contribution to the interaction energy, at mid- to long-range separations[16–18]. For example of the inability of traditional GGA functionals to capture weak interactions means that the attraction between layers of graphene cannot be recovered with these functionals. Recently attempts have been made to address this limitation[19] either through the incorporation of empirical correction terms[20] or by using functionals that incorporate genuine nonlocal contributions to the correlation functional.[21,22]

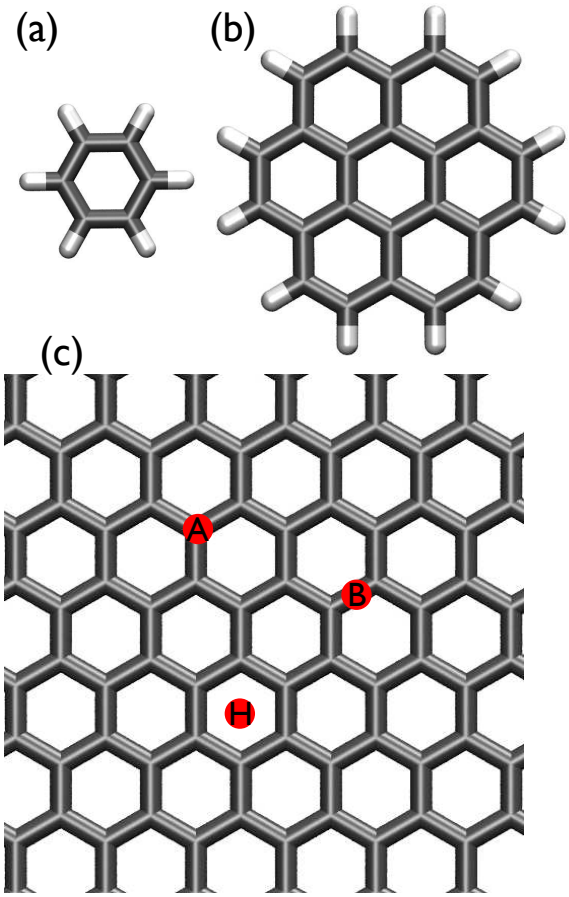

Fig. 1 The arene ring systems (a) benzene and (b) coronene used in WFT based QM calculations and (c) a graphene sheet. The three binding locations on the graphene sheet, atop, bridging and hollow are marked by A, B and H, respectively.

Fig 2 shows the results of a study[23] that reported calculation of the interlayer binding energy of graphene sheets as a function of separation distance for the LDA, GGA, PBEsol[24] and five different functionals that account for the nonlocal contributions of the correlation function.[21,22,25,26] The LDA functional (which comprises the Slater exchange functional and

Table 1 Adsorption energies, E_{ads}, and separation distances, d_{sep}, in parantheses, to graphene of the reference molecules for the various functionals. Adapted from Ref.[8]

Abbreviation	Technique	Description
BOMD	Born Oppenheimer molecular dynamics	A type of FPMD
CC	Coupled cluster	A WFT-based method for QM calculations
CPMD	Car-Parrinello molecular dynamics	A type of FPMD
DFT	Density functional theory	One of main theories used for the QM calculation of molecular systems
DFTB	Density functional tight-binding	A QM approach that yields an approximation of the Kohn-Sham energy
FF	Force-field	A series of potentials used to provide a classical description of the PES of a system
FPMD	First-principles molecular dynamics	MD simulations in which the electronic degrees of freedom are calculated
GGA	Generalised gradient approximation	A class of approximations that are used for a type of DFT functional more sophisticated than LDA
LDA	Local density approximation	A class of approximations that are used for a type of DFT functional
MC	Monte Carlo	Simulation method in which the PES is sampled by the random generation of configurations, that are accepted or rejected based on the Metropolis Criterion
MD	Molecular dynamics	Simulation method in which the PES is sampled by the solving of Newton's equations of motion
PBE	Perdew-Burke-Ernzerhof functional	A DFT functional based on the GGA
PBEsol	PBE solid	A refinement of the PBE functional to better describe solid systems
SAPT	Symmetry-adapted perturbation theory	One method of calculating the noncovelent interaction between molecules
QM	Quantum mechanics/mechanical	A description of an molecular system in which the electronic degree's of freedom are explicitly described.
QMC	Quantum Monte Carlo	An alternative QM approach to WFT and DFT, based on using MC methods
WFT	Wave function theory	One of main theories used for the QM calculation of molecular systems, based on post-Hartree-Fock techniques

the Vosko-Wilk-Nusair correlation functional) is well known to over-bind in the case of weak, non-covalent interactions, and in this case actually yields attraction between the graphene sheets, unlike the GGA. The PBEsol functional (a functional specifically designed to solid-state systems) does marginally better than the GGA functional but still significantly underbinds the interaction between the graphene sheets. In this study, the performance of the vdW functionals appears to form two categories. The revPBE-vdW[21] and vdW-DF2[25,26] functionals yielded binding energies that fall within the experimentally measured range but give an interlayer separation slightly larger than experiment. In contrast, optPBE-vdW, optB88-vdW and optB86-vdW functionals[22] can recover the separation between the graphite sheets, at the expense of a slightly overbinding the interaction.

This relationship between the adsorption energy and separation distance for the vdW functionals is not limited to graphene sheets, but is a more general feature of these functionals.[8,27] Berland *et al.*[27] investigated the adsorption of benzene to graphene, while Hughes and Walsh calculated the adsorption energies and geometries of a variety of small organic molecules to graphene.[8] In both studies it was found that there is an inverse relationship between the adsorption energies and separation distances.

The improved quality of the vdW functionals can be seen in Table 2 and Figure 3, where the adsorption energies of a number of small molecules to a graphene surface have been determined using four different vdW functionals, and compared against reference values. The reference values have been obtained from experimental work[29,30] or from very high quality density functional theory/coupled cluster (DFT/CC) calculations.[28,31] Compared with the PBE functional, all four functionals with nonlocal contributions show a huge improvement. DFT/CC is a hybrid *ab initio*-DFT method that overcomes the traditional limitations of DFT approaches.[28,31] Another possible strategy for ensuring a better description of the weak interactions is to use symmetry-adapted perturbation theory DFT (SAPT-DFT).[32,33] Both DFT/CC and DFT-SAPT have been used to investigate the behaviour of graphene systems.[28,31,34–37] Quantum Monte Carlo (QMC) studies of lithium insertion into graphite structures have also shown that functionals with an improved description of the dispersion interactions outperform traditional functionals.[38]

While a QM description of a system can provide a great deal of information, in practice, the computational expense of such models means that they are often more likely to be used to calculate the properties of a configuration, or set of configurations, rather than within a simulation, where an ensemble of configurations is generated. First-principles MD (FPMD), such as Car-Parrinello[39,40] and Born-Oppenhimer (CP or BOMD) simulations enable the MD simulation of systems that include the electronic degrees of freedom, although

Table 2 Adsorption energies, E_{ads}, and separation distances, d_{sep}, in parantheses, to graphene of the reference molecules for the various functionals. Adapted from Ref.[8]

Index	Molecule	E_{ads} / kJ mol^{-1} (d_{sep} / Å)					Reference
		PBE	revPBEvdW-DF	optB88-vdw-DF	vdW-DF2	vdW-DF-C09	
1	Methane	-0.9 (3.88)	-16.6 (3.53)	-17.0 (3.43)	-14.1 (3.43)	-17.4 (3.32)	-13.5[a] (3.31[a])
2	Ethane	-1.5 (4.22)	-23.7 (3.69)	-25.7 (3.51)	-20.6 (3.65)	-26.6 (3.44)	-20.8[a] (3.44[a])
3	Hexane	-2.5 (4.32)	-56.6 (3.78)	-63.2 (3.60)	-50.5 (3.71)	-64.4 (3.52)	-51.0[b]
4	Ethene		-22.6 (3.52)	-24.9 (3.29)	-19.3 (3.37)	-26.2 (3.20)	-20.2[a] (3.24[a])
5	Benzene	-1.7 (3.41)	-46.9 (3.59)	-54.4 (3.33)	-41.4 (3.52)	-57.3 (3.24)	-43.1[a], -48.2[c] (3.30[a])
6	Toluene	-2.5 (4.32)	-57.6 (3.60)	-66.5 (3.36)	-50.7 (3.50)	-69.2 (3.28)	-56.5[b]
7	Ethyne		-19.7 (3.49)	-21.4 (3.31)	-17.2 (3.46)	-22.1 (3.24)	-17.1[a] (3.26[a])
8	Water	-2.3 (3.69)	-13.2 (3.51)	-13.8 (3.34)	-12.0 (3.35)	-14.1 (3.28)	-13.5[a] (3.19[a])
9	Ethanol	-2.2 (3.78)	-29.9 (3.33)	-32.0 (3.10)	-26.3 (3.24)	-34.1 (3.03)	-30.5[b]
10	Acetone		-37.4 (3.28)	-43.1 (3.09)	-34.1 (3.18)	-45.5 (3.05)	-34.3[b]
11	Ammonia	-1.3 (3.97)	-13.4 (3.65)	-13.5 (3.58)	-11.4 (3.52)	-14.2 (3.58)	-13.5[a] (3.31[a])
12	Acetonitrile		-29.9 (3.44)	-31.4 (3.18)	-26.2 (3.33)	-33.2 (3.17)	-31.8[b]
13	Ethyl Acetate		-51.2 (3.48)	-57.5 (3.22)	-45.6 (3.37)	-60.0 (3.16)	-48.1[b]

[a] DFT/CC calculation[28]; [b] Experimental[29]; [c] Experimental[30].

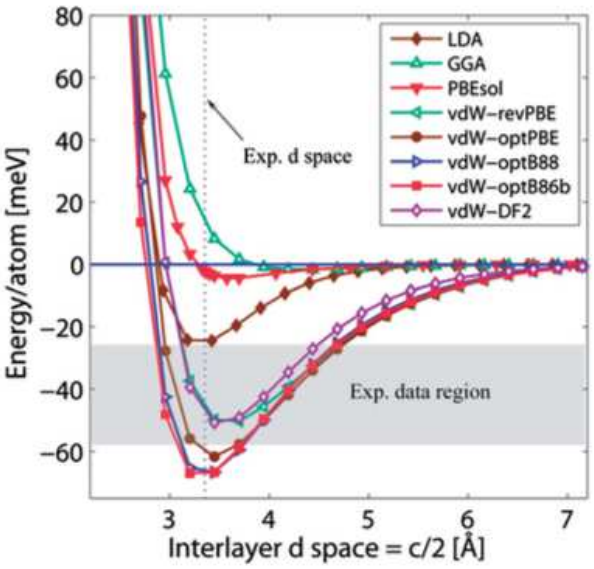

Fig. 2 The interlayer binding energy of graphite as a function of interlayer separation, d, as determined from a variety of different DFT functionals. Taken from Ref.[23]

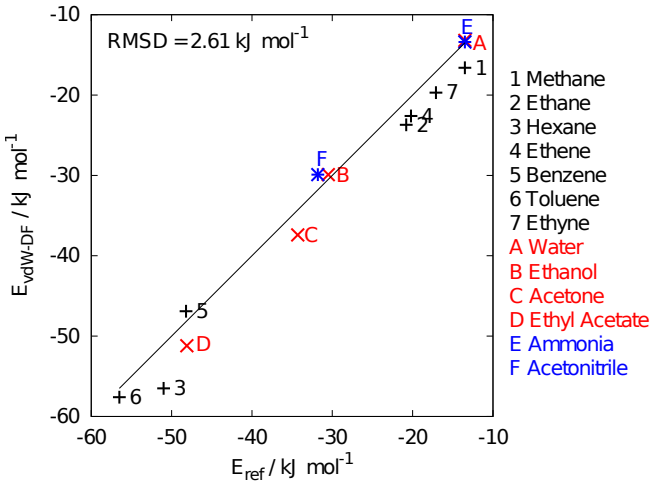

Fig. 3 Comparison between the reference adsorption energies for a set of small molecules adsorbed onto a graphene surface and those calculated with the revPBE-vdW-DF functional. The hydrocarbon, oxygen-containing and nitrogen-containing adsorbates are marked as the black, red and blue points, respectively. Taken from Ref.[8]

such simulations are limited to short time- and length-scales (tens of *ps* and Å). For graphene systems CP/BOMD simulations have *e.g* been used to study graphene-aqueous interfaces,[41–43] the formation of graphene sheets on metal surfaces[44–46] and the effects of doping on a graphene sheet on a SiO_2 substrate.[47,48]

Density functional tight-binding (DFTB)[49,50] is a fully quantum-mechanical approach that yields an approximation of the Kohn-Sham energy, while being more economical in terms of computational resource compared with solving the Kohn-Sham equations in the conventional manner. In a MD context, the DFTB approach allows the consideration of relatively larger system sizes (number of atoms in the system) and longer trajectories compared with first-principles MD. Examples relevant to energy materials include the study of transition metal clusters adsorbed on graphene[51], charge transfer at aqueous graphene interfaces[52], and the stability of graphene defects in the presence of adsorbed water[53].

The limitations of the time- and length-scales that are practicable with a QM treatment makes QM unsuitable for the study of a number of systems and properties. If data about the behaviour of a system over *ns* or hundreds of Å were required, a less computationally expensive model to describe the system is essential. This can be done through the use of a force-field (FF), where the interactions between different sites within the system are described through inter-site potentials. In an *atomistic* FF, each site will correspond to an atomic site within the system. To describe a system appropriately, a FF must be parametrised; typically this parametrisation is made using data obtained from either experiments and/or QM calculations. Each FF will be parametrised for a certain set of systems/molecules (a fitting set); one well-known limitation of a FF representation is its transferrability. If a FF is used to model a system that is too dissimilar from that which was used in the parametrisation, the results may not be meaningful. As such, choice of which FF to use in any molecular simulation should be made with care.

Traditionally, atomistic FFs capture the electronic degrees of freedom implicitly. This can be a limitation in the case of graphene, which is a highly conductive material. To overcome this limitation a number of FFs have incorporated a description of atomic polarisation. Simple descriptions of polarisability include the rigid-rod dipole[54] and core-shell[55] (or Drude oscillator) models. A more rigourous description of polarisation is that used in the AMEOBAPRO FF[56–59]; this model of polarisation was partnered with a high-quality description of the electrostatics via the distributed multipole approximation.[60,61]

Another possible variation of FFs is whether they are *reactive* or not. A reactive FF can capture the dynamic formation/destruction of covalent bonds, while in a conventional, non-reactive FF the number and type of bonds remains fixed throughout the simulation.[62,63] Reactive FFs that have been used for graphene simulations include the ReaxFF developed by van Duin and co-workers,[64–66] the reactive bond order/adaptive intermolecular reactive bond order (REBO/AIREBO) potentials, and the charge-optimised many-body (COMB) potential.[67,68] The drawbacks of reactive FFs are that they typically have a higher computational cost compared with conventional FFs, often require a more complex parametrisation procedure. These FFs typically have a large number of parameters, and this can lead to difficulties in obtaining physical insights from the results generated by these FFs.

Ultimately it is vital to select the most appropriate techniques to study a system computationally, just as in experimental work. The choice of technique, structural model and FF should be made with care.

Graphene-aqueous interfaces

Typically, water is not one of the primary species that is intentionally present in systems designed for energy applications. However, the ubiquitous presence of water means that even, or especially, in anhydrous systems the effect of water as a should be considered. As such, we give a brief overview of computational investigations the interaction of water with the graphene surface.

The aqueous-graphene/graphite interface has been studied in some detail, at both the force-field[69–82] and quantum[41–43] levels of theory. While there is general agreement on a number of criteria, *e.g.* the position of the peaks in the vertical density profiles (see Fig 4), other characteristics, such as the orientation of the O-H bonds at the interface, are not as clearly resolved.

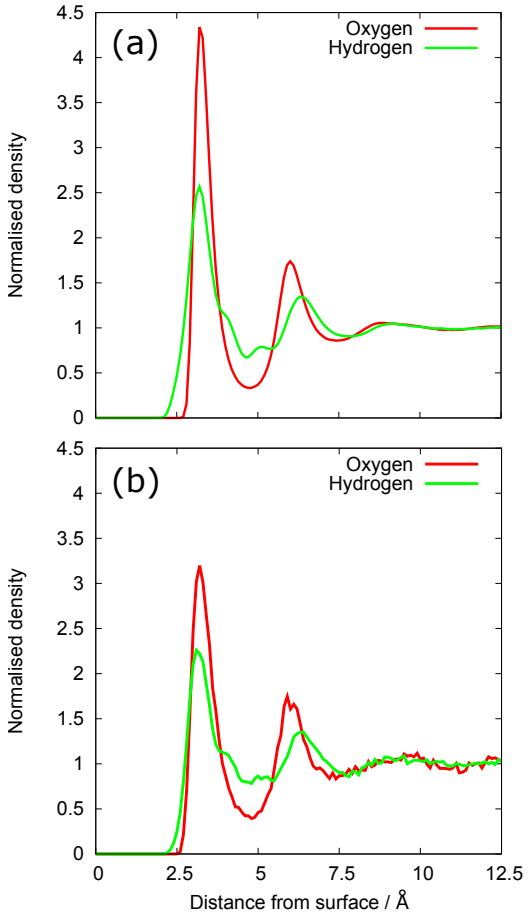

Fig. 4 Interfacial density profiles of graphene-water interface calculated using a) the GRAPPA FF[8], and b) the AMOEBAPRO FF[56,59]. Adapted with permission from Ref[8].

A number of studies have investigated the importance of explicitly including polarisation in FFs used to model the in-

terfaces of graphitic nanostructures with water.[77,79,83–86] Zhao and Johnson derived a FF that incorporated polarisability via atomic quadrupoles on graphite and water.[83] These authors found that for weakly polar fluids the polarisation contributions were negligible compared with the Lennard-Jones (LJ) interactions. However, for strongly polar fluids, such as water, the contribution from the polar terms to the total potential energy was found to be significant. The first MD simulation using a polarisable nanotube immersed in liquid water was done by Moulin *et al.*,[84]; the FF comprised a LJ term between the carbon and oxygen and an electrostatic term between charges on water and the induced dipoles on the polarisable nanotube, with the TIP4P potential for water.[87] Despite the fact that CNTs have a very large polarisability, they concluded that the influence of the nanotube polarisation was negligible on the arrangement of the water molecules around the nanotube and on their adsorption energy. Sala *et al.* investigated how the interface of graphene with aqueous NaCl solutions changed when polarisability was incorporated into their FF (where only the salt ions and water molecules were treated as polarisable). This study found that the accumulation of ionic species at the graphene surfaces was greater for the polarisable than the non-polarisable FF. In a recent study which simulated a polarisable water model interacting with a polarisable graphene surface,[79] polarisablity enhanced the number of water molecules with an O-H bond oriented towards the surface. In determining the adsorption energies of ions with a graphene surface *in vacuo*, Schyman and Jorgensen reported that polarisation was essential.[86]

Simulations of Electrolytes at Graphene Interfaces

The interaction of electrolytes at graphene interfaces has implications for graphene based energy applications.[88] Mixed carbonate electrolytes, containing such species as ethylene carbonate (EC) and dimethyl carbonate (DMC), are used as electrolytes in commercial lithium ion batteries (see Section 'Lithium/Alkali Metal Batteries'). While ionic liquid (IL) electrolytes have been suggested as potential components of both supercapacitors,[89] and alkali metal ion batteries.

The majority of simulation studies on IL electrolytes interacting with graphene surfaces[89–104] have used MD to predict the interfacial structure of electrolyte solutions.

In all cases the structuring, both translational and orientational, of the IL electrolytes normal to the graphene electrodes is observed, typically extending $\sim$ 20-30 Å from interface.[90,91,94,105] The exact nature of this structuring of the species in the electrolyte solution depends on a range of factors, including the charge of the electrodes, the chemical composition of the electrolytes, the presence of dopants and the FF used for the simulations. Kislenko *et al.*[90] found that in addition to the structuring normal to the interface there was a 2-D hexagonal lateral ordering of ions at an uncharged substrate, though other studies have not reported a similar observation. Using the polarisable APPLE&P FF[106,107], Vatamanu *et al.* found that as the charge on the electrodes was increased, there was a build-up of counterions at the electrode and decrease in co-ion population in first adsorbed layer.

Shim *et al.*[92,108] used MD simulations to compare the differences between an electrolyte consisting of a pure room temperature IL, [EMI][PF_4], and an organic electrolyte doped with the same IL, 1.1 M [EMI][PF_4] in acetonitrile. It was found that the ion-conductivity of the electrolyte solutions depended upon the system setup. In systems containing a double-sided electrode the ion conductivity was greater for the mixed RTIL/organic than for the pure RTIL electrolyte.[108] In a system having a parallel plate configuration the opposite result was true.[92] The authors also observed a a strong cathode/anode asymmetry in capacitance for the parallel-plate configuration. This was attributed to the more efficient screening of the electrode charge by [BF_4] compared with [EMI]. Likewise 'through graphene' screening effects enhance and reduce the screening of the cathode and anode, respectively, in the double-sided electrode configuration.

Lyndell-Bell and co-workers reported a number of studies on the behaviour of IL electrolytes at graphene interfaces.[94,105] They investigated the effects of screening at uncharged, positively and negatively charged graphene interfaces for a solution of [DMIM][CL] (using the OPLS FF, *i.e.* a non-polarisable FF) by calculating the potential of mean force (PMF) profiles of different probe molecules with the graphene interface. Both the charge and size of the probe was varied. They summarised the structure of the ions at interfaces as shown in Fig 5. At the cathode there is a dense layer of [DMIM] counter ions, which are oriented such that the long axis of the molecules is parallel to the plane of the substrate. This in turn is followed by a layer of chloride co-ions and a further less dense layer of co-ions that is less orientationally ordered. At the uncharged wall both cations and anions are present in the first layer molecules, but the density of cations is greater than that of the anions. At the anode the chloride ions form a dense first layer at the wall, there is then a layer of co-ions orientated parallel to the plane of the interface. This difference in the structuring to ions at the cathode and anode causes significant asymmetry in the interactions of probes with charged walls. Indeed two of the findings are rather counterintuitive, (1) the free-energy minimum for a positive probe in contact with a negative wall was higher in free-energy than the minima when the probe was embedded in the second layer of ions and (2) that a minimum in the free-energy profile of a negative probe near a positive graphene surface was lower than the minima of a positive probe in contact with the same sur-

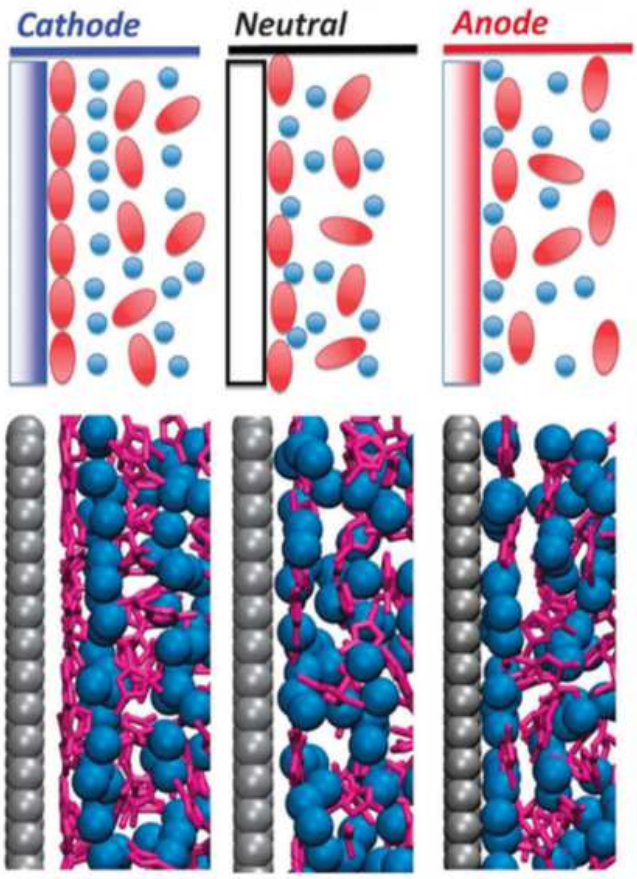

Fig. 5 Structure of [DMIM][Cl] at negatively, uncharged and positively charged graphene interfaces, shown in schematic form (top) and snapshots from the MD simulation (bottom). The [DMIM] cations are shown as red ovals or coloured pink, while the [Cl] anions are shown as blue spheres. Taken from Ref. [105]

face. The authors explained the reason for these results as due to the fact that the interaction of the probe with the solvent is more significant than the interaction of the probe with the wall. As the probe is effectively an ion itself; this implies that the solvent-solvent interactions dominate the solvent-electrode interactions. These simulations have recently been extended to investigate the interaction of IL electrolyte doped with alkali metal ions, ([BMIM][BF_4] doped with $LiBF_4$/$KBiF_4$) between charged graphene sheets using the OPLS-AA FF.[103] In agreement with their previous work, it was found that there were significant energy barriers for the Li^+/K^+ ions to diffuse to the cathode. At 10 mol % $LiBF_4$/$KBiF_4$ no lithium or potassium ions were able to diffuse to the negatively charged graphene electrode. Increasingly the concentration of salt to 25 mol % does allow Li^+ and K^+ cations to adsorb onto the cathode but even in this case the free-energy barrier for the metal ions to diffuse past the first layer of [BMIM] cations is considerable ($\sim 20k_BT$). Again, this indicates the dominance of the ion-ion interactions over the ion-electrode interactions in these simulations.[94,105]

Classical MD simulations have also been used to investigate the structure of carbonate based electrolytes doped with lithium salts, most commonly $LiPF_6$, at graphitic interfaces.[97,109–112] Vatamanu *et al.* found that the composition of the electrolyte interfacial layer depended strongly on the electrode potential. The amount of EC and DMC at the interface increased as the electrode charge was increased, for both positively and negatively charged electrodes. In contrast with the work of Mendez Morales *et al.*[103] studying lithium doped IL electrolytes (see above), both Vatamanu *et al.* and Xing *et al.* have found that Li^+ was able to accumulate at the negative electrode in carbonate electrolytes.[97,111] However, it was found that the structure of the EDL at the interface depended strongly on both with electrolyte composition and applied potential. Thus the difference in the findings of the Vatamanu *et al.*/Xing *et al.* and Mendez Morales *et al.* studies may be explained as due to the difference of in the electrolyte compositions. An alternatively explanation is that in the study of Vatamanu *et al.*/Xing *et al.* the polarisability of the electrodes was explicitly modelled within the FF.

Abou Hamad *et al.* investigated the effect of using an oscillating electric field of a system consisting of an graphite anode and an electrolyte of EC, propylene carbonate (PC) and $LiPF_6$. The simulations showed that the oscillating electric field was able to reduce the average intercalation time, and that the dependence of the intercalation time on the applied field amplitude was exponential.

Recently Jorn *et al.* used MD simulations to investigate the structure of the solid electrolyte interface (SEI) of a EC/$LiPF_6$ electrolyte. The full electrode-SEI-electrolyte region was modelled, with the finding that as the thickness of the SEI was increased Li^+ ions were drawn closer to the SEI.

The majority of MD simulations of electrolytes have tended to use non-polarisable FFs, although there are a few exceptions.[91,93,96–98,104] Unfortunately, to the knowledge of the authors there has not been a systematic study of the effect of polarisation on behaviour of electrolytes *at graphene interfaces*. As mentioned above a number of studies[94,103,105] have found that the ion-ion interactions tend to be of greater importance then the ion-graphene interactions. However, this may be due to the fact the polarisability of the graphene substrate has not been accounted for in the models. One would predict that use of a FF that explicitly includes polarisation of the graphene interface would identify a greater importance for the ion-graphene interactions. For example, in the GRAPPA FF[8] the polarisation contribution of the *in vacuo* adsorption energy of a charged amino-acid and a counter ion is ~ 50 %.

While the size of the systems simulated typically makes

FF-based models more appropriate, there have been a number of FPMD simulations of graphitic-electrolyte systems.[113–115] Leung *et al.* have used FPMD simulations to investigate the initial stages of the SEI formation on graphite anodes of lithium ion batteries.[114,115] The carbon edge termination of the graphitic anodes was found to play a major role in affecting EC decomposition. Ganesh *et al.*[38] reported FPMD simulations of the SEI of $LiPF_6$ in EC, DMC and PC electrolytes, as well as for different anode surface terminations. It was found that PC was more readily reduced than DMC and EC, with Li_2CO_3 being an important component of the SEI. The formation of LiF, and its agglomeration at the interface was also observed. The reduction of the carbonates was heightened at O or OH terminated surfaces. While the computational cost of such simulations are limited to short time- and length-scales, they revealed insights on the reduction processes that occur at the SEI.

Photovoltaic Applications and the Electronic Structure of Graphene

There has been considerable interest in the utilisation of graphene within photovoltaic devices, such as organic photovoltaic cells (OPVs) and dye-sensitised solar cells (DSSCs).[116,117] Theoretical studies for these applications have typically investigated the electronic proprieties of graphene structures, since the majority of the publications in this area have reported use of QM calculations.[47,48,118–122]

Much of the interest of graphene for photovoltaic applications is due to its high charge-carrier mobility.[117,118] This is despite the fact that graphene is a zero-band gap semiconductor (*i.e.* the density of states (DOS) is zero at the Dirac point). The high carrier mobility observed in graphene is due to the fact that the sheets will be usually be doped, as even mere exposure to moisture and air can moderately dope graphene.[123,124] The presence of dopant species will mean that the Fermi level will not residue at the Dirac point of the graphene film and that charge will flow through the film. While graphene films exposed to air will show this effect, the charge carrier concentration can be increased by further chemical doping, which will reduce the resistance of the film further.[118]

The doping of graphene films by substrates,[48,125–133] non-covalently adsorbed molecules,[47,122,134–138] or the insertion of B/N atoms into the graphene film[139–142] can either induce charge *transfer* from the graphene, *p* or hole doping, or *to* the graphene, electron or *n*, doping. Manipulation of band-gap properties is central to advancing developments in photovoltaics.

Considering the effect of the substrate first, there have been a number of theoretical studies that have investigated graphene on silicon carbide, SiC.[126,127,143,144] First-principles calculations have shown,[123,126,127] in agreement with experimental data,[145,146] that the first layer of graphene will covalently bond to the SiC substrate. This will induce *n*-doping of that layer of graphene but with further layers of graphene having the same electronic behaviour as isolated graphene sheets. The facet of the substrate also affects the electronic behaviour of the system, with graphene overlayers on SiC(0001) and SiC(000$\bar{1}$) being metallic and semiconducting, respectively.[126] Kim *et al.* investigated the covalent bonding between the substrate and graphene overlayer in more details by using a large supercell, finding the systems split into different regions.[143] In those regions where there is alignment of the lattices, covalent bonding occurred, while outside these regions there were boundaries where the C atoms moved away from the substrate. Overall this produces a hexagonal pattern on covalently bonded regions.

SiO_2 is another substrate whose effect on graphene has been investigated theoretically.[129,132,133,147] On pristine hydrogen-passivated SiO_2 there is alignment of the Diarc point with the Fermi level indicating that no doping occurs.[48,129,132] However, experimental data obtained Raman spectroscopy has shown that SiO_2 can induce doping.[148,149] Using FPMD simulations, Nistor *et al.* have showed that *certain* defects in the SiO_2 substrate are able to induce doping and charge transfer.[48] The introduction of a silicon vacancy at the interface will not cause doping the the graphene layer, as the atoms around the defect site will quickly re-arrange to self-passivate the defect. However, if the defect centre contains a dangling bond the system is unable to terminate the bond (at least on the time scales accessible to the simulations) and *p* doping occurs. If boron or phosphorous impurities are present within the substrate then strong doping can occur with graphene being *p*- or *n*-doped, respectively.

One substrate which has prompted particular interest is hexagonal boron-nitride (hBN).[125,147,150–154] Theoretical studies have shown that a band gap is present in graphene-hBN bilayer systems,[125,150,153] and that this gap can be tuned by changing the interlayer spacing and stacking arrangement.[151,152] However, experimental studies have had difficultly finding such a band gap.[153] Karche *et al.* argued that this discrepancy could arise from the fact that while the perfectly Bernal/AB stacked graphene/hBN (where half of the C atoms are positioned exactly above the B atoms) does show a band gap, misaligned graphene overlayers have no band gap.[153] As well as investigating the effect of a bulk hBN substrate, DFT calculations have also been used to study the properties of graphene/boron-nitride hetrobilayers (C/BN HBLs).[152,154] For these systems, both the AA and AB stacked bilayers produce a band gap, with the AA arrangement always giving larger gap for the same interlayer distance.[152,154] This was reasoned as being due to stronger orbital interaction lead-

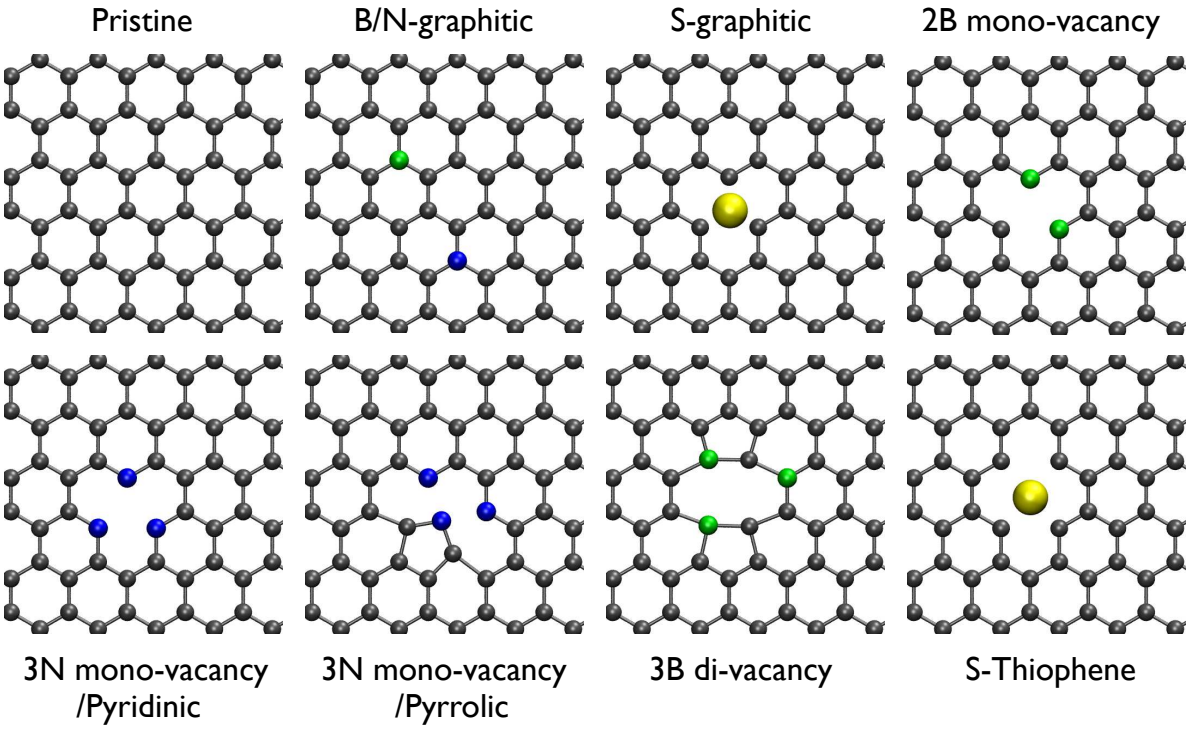

Fig. 6 Representative examples of the different types of doping in graphene. The carbon, nitrogen, boron and sulphur atoms are coloured grey, blue, green and yellow, respectively.

ing to stronger charge transfer for the AA arrangement.[154] It has also been shown that it is possible to tune the band gap of C/BN HBLs, theoretically, by functionalising the h-BN sheet with hydrogen and fluorine.[147]

The incorporation of B or N atoms into lattice is another way to dope graphene.[139–142,155,156] The swapping of a single C atom for a B atom or a N atom will shift the Fermi level downwards (*p*-doping) or upwards (*n*-doping), respectively. Surprisingly, however, the charge density distributions on singly doped B and N defect are the opposite of what would be expected from their classification as *p*- or *n* dopants. The N atom actually gains charge while the B atom loses charge to the graphene sheet. The reason for this apparent inconsistency arises from the fact that in order to retain the aromaticity of the lattice the dopant atoms are required to have a half filled p_z orbital. At the same time there is an unequal sharing of electrons in the sp^2 σ-bonds of the dopant atoms and the adjacent C atoms.[141] In addition, to single substitutions more complex systems have also been studied, including triple substitutions with a vacancy (also called pyridinic, see Fig. 6)[141] and multiply-doped systems.[140,156] The effect of nitrogen doping through the covalent bonding of N-containing aromatic species, *e.g.* pyridine, pyrimidine, etc, has also been investigated.[142]

Doping graphene with non-covalently adsorbed molecules rather than covalent bonding species offers a number of advantages, in that it does not perturb the lattice and is also reversible.[122,157] Hu and Gerber recently investigated the non-covalent doping of graphene sheets by tetrathiafulvalene (TTF) and tetracyanorethylene (TCNE), comparing the effect of the LDA, PBE and vdW-DF functionals.[122] They found that by including the nonlocal correlation terms (via the vdW-DF functional) the strength of the binding between the dopants and the graphene sheet was significantly increased over not only the PBE but also the LDA functional. They also compared the effect of functional on the degree of charge transfer between the molecules and the graphene monolayer. For TTF they found that the behaviour of the two GGA functionals was very similar, but there was a significant difference with the LDA results. LDA was found to overestimate the charge transfer, which the authors explained as due to the LDA functional's intrinsic tendency to delocalise electron density. This 'over-delocalised' electron density results in a large overlap of the electron density of the two species and a larger charge transfer. The authors concluded that in contrast to previous studies,[136,158] on the same system that low concentrations of TTF will not *n*-dope graphene. In contrast, they found that although the adsorption energies for TCNE differed with functional, the degree of charge transfer was largely unchanged at $\sim$0.46 e. This level of charge transfer had a significant effect

on the electronic structure of the graphene monolayer, with a shifting of the Fermi level. The *p*-doping of the graphene by the TCNE molecule was sufficient to make the substrate metallic. The interaction of both TTF and TCNE with the graphene substrate was mainly physisorption, emphasising the importance of using an appropriate functional, in DFT calculations of such systems, *i.e.* one that captures weak non-covalent interactions.

Nistor *et al.* used FPMD simulations to investigation the interactions of two *p*-dopants, to advance the theory that the charge transfer in surface-doped graphene systems is driven by a 2D surface-induced electronegativity equalisation principle (2SEE).[47] In this process graphene acts as a 2D surface catalyst on which the disproportion of adsorbed dopants into charge transfer complexes is facilitated, these complexes then dope the graphene. To validate this theory, first-principle simulations of two molecular *p*-doping species, $SbCl_5$ and HNO_3, as well as the compound $AlCl_3$ between two graphene sheets were reported. Graphene induced disproportionation of all three molecules was observed with the formation of open shell complexes. Once dissociated species had formed, an opening in the bad gap was indeed observed.

The ability of theoretical methods to investigate the electronic structure of graphene under different conditions is vital to both providing us with a greater understanding of the processes occurring as well as assisting in the development of new (nano)-electronic and photovoltaic applications.

Fuel Cells

Polymer electrolyte fuel cells (PEFCs) possess significant future potential as alternatives to fossil-fuel based solutions for efficient energy conversion. Currently, these fuel cell technologies are not competitive when judged over a range of metrics including cost, reliability and durability. One of the key reactions in PEFCs is the oxygen reduction reaction (ORR), which takes place at the cathode. This reaction is widely recognised to be the kinetic bottleneck in the fuel cell, being very sluggish compared with the corresponding reaction at the anode. The best performing Pt/C fuel cell catalysts facilitate efficient ORR, which is thought to be most efficient when it proceeds via the 4-electron mechanism:

$$O_2 + 4H^+ + 4e^- \longrightarrow 2H_2O$$

At present, the presence of platinum is considered to be essential for the efficiency of this process.

From a commerically-viable perspective, these Pt/C catalysts remain uncompetitive with fossil-fuel based energy solutions because they suffer from serious drawbacks, due to several factors. These include: the gradual sintering of Pt nanostructures with time that leads to Pt agglomeration, losing surface area and thereby loss of the catalytic activity; the Pt nanostructures are highly susceptible to catalyst poisoning;

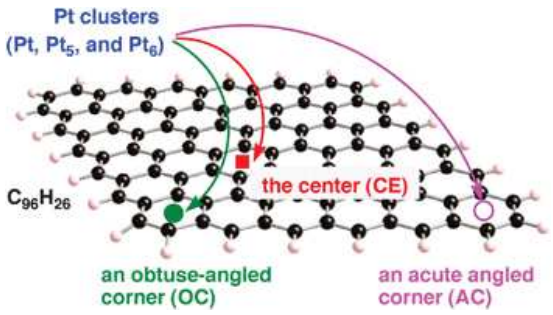

Fig. 7 Possible adsorption sites on a hydrogenated graphene nanoflake ($C_{96}H_{26}$) for Pt nanoparticles. Taken from Yumura *et al.* [159].

Pt itself is very expensive, thus from a cost perspective it is highly desireable to limit or eliminate the dependence of fuel cell devices on Pt. The challenges to reduce the dependence on Pt in these PEFC catalysts, while retaining device durability is significant; the US Department of Energy has set targets that state that by 2017 the total Pt loading of a fuel cell device (both electrodes) must be reduced below 0.125 mg cm^{-2} and must deliver 5000 hours of stability under simulated operational conditions [160].

The carbon support for these Pt/C devices has also been the subject of intense scrutiny. Graphene, with its high surface-area-to-mass ratio, superior charge-carrier mobility, high tensile strength and excellent thermal conductivity, is an ideal candidate for this purpose. For this reason, in recent years, considerable effort has been directed at the use of graphene-based materials, in a search to either limit, or, entirely eliminate, the dependence on Pt for delivering ORR efficiencies and increased durability in PEFCs. Graphene has been exploited as a support substrate for Pt (and other metal) clusters for ORR catalysis, while *doped* graphene has been shown to capable of functioning as the catalytic material itself. In working towards meeting these goals of advancing the efficiency, economy and durability of PEFCs, computational techniques have made valuable contributions to the advancement in this field in several arenas. In this section, we will review use of computational chemistry and modelling in this area.

The investigation of undoped graphene as a support material for Pt-based fuel cell catalysts has benefited substantially from quantum chemical calculations, principally using density functional theory (DFT). One focus of such studies has been the sintering mechanism of the graphene-adsorbed Pt nanoparticles (PtNPs), which could conceivably take place either via coalescence or Ostwald ripening [161]. Yumura *et al.* [159] considered finite-sized hydrogen-terminated graphene flakes and used both real-space DFT calculations with traditional functionals (the hybrid B3LYP [162] and LDA [163,164]) and modest-sized basis sets, and fully-periodic plane-wave DFT (PW-

DFT) calculations (with the PW91 functional[165]), to calculate the structure and energetics of surface binding of Pt, Pt_5 and Pt_6 on graphene (see Fig 7). Unlike many other studies of PtNP adsorption, these authors considered a range of possible PtNP configurations. Their findings suggested that PtNPs could be pinned at the hydrogen-terminated graphene edges.

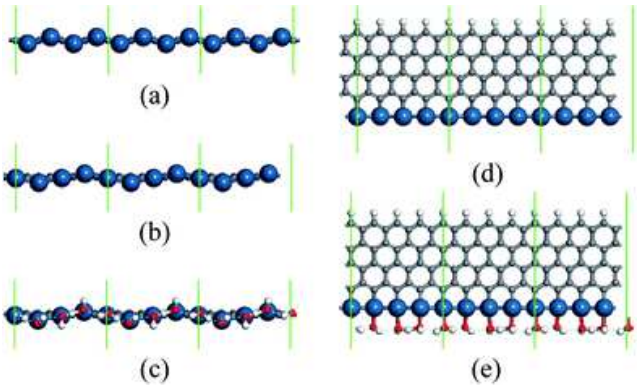

Fig. 8 Structures of the bare and water/OH decorated Pt-wire adsorbed on a graphene edge. Gray, blue, white and red colors denote C, Pt, H and O atoms. (a) is the side view of the bare structure from Soldano *et al.* [166], (b) and (c) are the side view of the bare and solvated structures in this work while (d) and (e) are the corresponding plan views, respectively. Taken from Xiao *et al.* [167].

Besides a propensity for agglomeration, Pt-based catalysts also have a drawback due to high costs and ever-decreasing availability of raw materials. Use of alloyed metal NPs are one viable strategy for decreasing this reliance on the availability of Pt. In a study chiefly focussed on the experimental process of making high quality graphene sheets decorated with PtNPs, free from surfactants and halide ions, Qian *et al.* [168] also reported use of PW-DFT calculations with the PBE functional[169] to probe how adsorption of PtNPs and alloyed NPs (Pt/Pd) on pristine graphene affected the electronic structure of the nanoparticles.

Very little has been reported to date regarding the use of force-field based molecular dynamics (MD) simulations in this particular area. However, recently Xu *et al.*[170] complemented their extensive microscopy-based evidence of PtNP self-organization on freestanding pristine graphene sheets with such MD simulations, using the reactive force-field ReaxFF[64–66].These simulations indicated a strain-based mechanism of PtNP lateral self-organisation, resuting in flattened PtNP shapes that were elevated above the suspended graphene substrate rather than being partially encapsulated by the graphene. The dimensions of the resulting self-organised PtNPs was consistent with their experimental results. The possbility of covalently anchoring metal NPs to the graphene surface, *e.g. via* surface functionalization, such as was reported recently for tethering of PdNPs onto graphene oxide, using benzyl mercaptan linkers[171] could prove to be a useful strategy for immobilisation of Pt-containing NPs for ORR catalysts.

Besides a propensity for PtNP sintering, another general disadvantage of Pt/graphene based PEFCs is the propensity for CO poisoning of the PtNPs. One key concept that is central to much of the current literature in the study of catalytic activity for metal-based systems, with respect to the propensity for CO poisoning as well as the efficiency of the ORR, is the energy of the *d*-band centre (ε_{dc}) of the metal atoms; Nørskov *et al.* [172] had found that for pristine Pt surfaces, the Pt atom *d*-band centre was strongly correlated with the adsorbate binding strength. Considering pristine graphene as a substrate, Kim *et al.* [173] presented PW-DFT calculations using the PBE functional of small Pt_n (n =1,2,4) clusters on *strained* graphene. The applied strain was found to enhance to the PtNP binding to the surface, thus improving the thermal stability of the catalyst. These authors also found that strain delivered a lower ε_{dc}, most notably for the Pt atoms in immediate contact with the graphene substrate. This effect was related to the calculated adsorption energies of H_2, CO and OH adsorbates. The CO oxidation reaction pathway was also explored (including barrier calculations via transition-state optimisation) for Pt_6. Imposing strain on the graphene was found to lower the barrier of the rate-determining step in this process. As a recent and different way of approaching this problem, Xiao *et al.* [167] explored the catalytic behaviour of a Pt nanowire adsorbed along the edge of a graphene nanoribbon substrate (see Fig 8). Building on an earlier study[166], and using periodic PBE calculations, the authors calculated the free energy of binding of key ORR intermediates at the nanowire, indicating the viability of this substrate configuration.

By far the greatest number of reports in the literature regarding the computational exploration of graphene as a support material for PtNPs has considered doped, rather than pristine, graphene[174,175]. While the majority of these studies have focused on nitrogen, other dopants, such as B, O, P, and Be have also been investigated. Acharya and Turner[174] applied real-space B3LYP calculations to hydrogen terminated grapene flakes (with 66-69 carbon atoms) and calculated formation energies with N, P, B, Al and Si dopants. Their calculations of the binding energies of Pt atoms and Pt_n clusters ($n = 2,5$) at these doped sites for B and N, indicated that binding at B sites was strongest, and they also investigated the impact of higher B concentration on binding. Their data indicated that this enhancement in binding did not descrease with Pt cluster size. In a later study, Acharya and Turner[175] also considered an alloyed Pt (PtRu), in the presence of an electric field. This cluster was found to adsorb more strongly than the corresponding Pt cluster on B-doped graphene. This was further explored by Acharya *et al.* [176] via PW-DFT PW91 calculations of Pt clusters (Pt_6, Pt_{10} and Pt_{32}) and Pt/Ru NP al-

loys (Pt_2Ru_4 and Pt_4Ru_6) on N-doped, B-doped, and co-doped graphene surfaces. One of the outcomes from this work was a fitted Lennard-Jones Pt/graphene force-field (FF), based on their first-principles data. Again, these authors predicted that the alloyed clusters had superior stability to their pure Pt counterparts, and that B-doped graphene yielded the highest adsorption strength. However, in all three instances, the authors did not consider a wide variety of possible cluster structures, such as was investigated by Ramos-Sanchez and Balbuena [177] for Pt nanoclusters on 3-sheet graphene substrates.

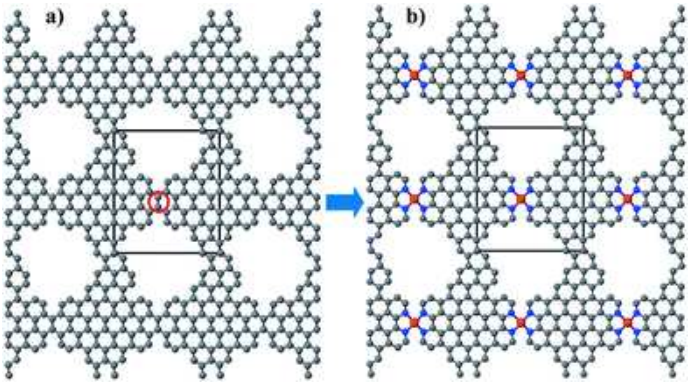

Fig. 9 Structures of a) graphitic pores, and b) MeN4 (Me = Fe, Co, or Ni) clusters embedded between these graphitic pores. Gray, blue, and brown spheres represent C, N and metal atoms, respectively. Rectangles enclosed with solid black lines show the unit cell used in the DFT calculations. Taken from Kattel and Wang [178].

Kim and Jhi [179] used PW-DFT calculations to investigate how doped graphene (either N-doped and B-doped) could facilitate stronger pinning of the PtNPs to the substrate, as well reduce the likelihood of CO poisoning. Their calculations revealed that the Pt ε_{dc} correlated well with the binding energies of both H_2 and CO on the graphene-supported Pt clusters. These authors also found that nitrogen-doped graphene (N-Gr) both increased the binding of PtNPs to the substrate and lowered ε_{dc}, thereby improving tolerance to the presence of CO. Tang *et al.* [180] also reported investigated the prevention of CO poisoning of the Pt_4 cluster adsorbed on both pristine and O-doped graphene via PW-DFT PBE calculations. These authors found that altering the charge of the Pt cluster from negative to positive could tune the CO binding strength from strong to weak. Groves *et al.* [181] probed the ability of dopants to deliver enhanced PtNP stability by reporting adsorption of a single Pt atom on pristine and doped (Be, B, N and O) graphene flake substrates 42 carbons) using real-space B3LYP calculations with modest basis sets. In agreement with previous calculations, B-doping was found to yield greater Pt stability than N-doping. However, both Be and O were found to perform even better, with the O-dopant delivering the strongest Pt adsorption.

Viewing the entire fuel cell process from a different perspective, Durbin and Malardier-Jugroot [182] used B3LYP calculations with modest basis sets on doped graphene flakes to investigate the possibility of using metal (Ni, Pt and Au/Ir) adsorbed on graphene as a membrane to clean H_2 feedstock fuel for the reaction at the fuel cell anode. The dopants were found to enhance binding between single metal atoms and graphene, while also showing reasonable binding selectivity between CO and H_2. O-dopants were found to work best in this respect, with Ir/Au performing better than Pt. Seo *et al.* [183] also investigated durability of Pt clusters on N-doped graphene substrates, with a 5.5% N-dopant concentration. Their PW-DFT PBE calculations agreed with previous work in that Pt atoms adsorbed more strongly to the N-doped surface compared with undoped graphene. The authors also predicted that the cohesive energy of the cuboctahedral Pt_{55} NP adsorbed via a $\{111\}$ facet would be enhanced on N-doped graphene relative to the pristine substrate. Recently, PW-DFT PBE calculations of the binding properties of sulful-doped graphene with respect to Pt atoms and PtNPs [184]. S-doped graphene led to relatively stronger binding of Pt atoms compared with the undoped case. The authors also reported the prediction of cohesive energies of Pt_{13} on both substrates, indicating superior PtNP stability on S-doped graphene.

The utility of doped graphene has also been explored via computational chemistry from the perspective of the stability of ORR intermediates at the graphene-supported PtNP interface. For the previously-mentioned N-doped graphene and pristine graphene systems reported by Seo *et al.* [183], these authors also used DFT calculations to evaluate the range of ε_{dc} for the surface-adsorbed Pt_{55} NP. These authors correlated these ε_{dc} values with the adsorption energy of an oxygen atom on the supported PtNP; oxygen binding was weakest for the N-doped graphene support, thus supporting the prediction that PtNPs supported by N-doped graphene could improve ORR kinetics. In a similar vein, Higgins *et al.* [184] explained the superior ORR kinetics of the Pt/S-doped graphene system via the calculated negative shift in ε_{dc} values for supported Pt_{13} compared with undoped graphene.

Graphene-supported metals (not substitutional dopants) other than Pt have been investigated with quantum chemical approaches, notably graphene-supported Fe and Co. Both bulk and edge locations were investigated as candidate sites for nitrogen doping, using PW-DFT PW91 calculations by Jain *et al.* [185]. These authors also used these calculations to predict the most likely edge site (on N-doped graphene) for adsorption of Fe atoms. However, these authors did not probe the adsorption of any ORR-relevant intermediates in this work. Vayner and Anderson [186] reported calculations of adsorption energies for key intermediates in the ORR for a substrate comprising a Co atom bound to an N-doped graphene flake. These data were used to predict reversible potentials for

ORR-relevant reactions on this substrate. They concluded that the Co-adsorbed system featured favourable reversible potentials for intermediate steps in the ORR. However, the calculated poor stability of the Co complex with N-doped graphene flake indicated this catalyst to be highly prone to rapid deactivation. Co-decorated undoped graphene was the subject of PW-DFT PBE calculations reported by Olson *et al.* [187], who investigated binding of key intermediates H_2O_2, O_2, CO, and N_2. The ordering of adsorption energies supported their proposal that the Co-based catalyst has selectivity for H_2O_2 over O_2, thus favouring a $2e^-$ path over the preferred $4e^-$ pathway. The influence of more than one N-doped graphene flake, covalently connected via oygen/cobalt linkages, on the activity of the ORR was investigated by He *et al.* [188]. Using real-space B3LYP calculations with modest basis sets, the authors reported optimised geometries of possible catalyst structures and proposed that the molecular orbital delocalisation on the Co atom could help explain the ORR kinetics experimentally observed for this system.

Fig. 10 Optimised structures (top and side view) of a structure resulting fromthe FeN4 moiety embedded in an extended graphene sheet. Grey, blue and cyan spheres represent carbon, nitrogen and Fe respectively. Taken from Szakacs *et al.* [189].

While replacement of graphene-supported PtNPs with less precious metals may form a viable alternative strategy for fuel cell development in future, significant research activity has instead focussed on the complete exclusion of metal clusters, by targeting engineered graphene (particularly substitutionally-doped graphene) as a catalytic material for ORR in itself. These materials will be referred to herein as carbon alloy catalysts (CACs).

Dopants in graphene are known to strongly influence the electronic structure of the material [190]. Significant activity in this area has been aimed at computationally elucidating the properties of Me/N/C catalyts (where Me is typically a transition metal atom). A range of metals were investigated as candiates for the MeN_4 site embedded in an infinite graphene sheet by Calle-Vallejo *et al.* [191], where Me=Cr, Mn, Fe, Ru, Co, Rh, Ir, Ni, Pd, Pt, Cu, Ag and Au. Using PW-DFT RPBE calculations, these authors predicted the free energy of key ORR intermediates at the catalyic site, and found that in general, the oxidation state of the metal should be $+2$ for best ORR performance. The use of Ni atoms coordinated by 2 or 4 nitrogen atoms, located in either graphitic or edge sites of graphene (using a graphene nanoribbon substrate), were investigated by Kattel *et al.* [192], using the same approach and functional as Calle-Vallejo *et al.* [191]. The ORR was predicted to most likely proceed at the edge sites, under alkaline conditions, and could be influenced by the presence of magnetism in the Ni-N_2 edge site.

The Me-N_4 motif (Me=Fe, Co or Ni), situated between graphene pores (see Fig 9), was assessed for ORR catalytic properties by Kattel and Wang [178], again using a very similar approach and the same functional as above. From the binding free energy of ORR intermediates, these authors elucidated a $4e^-$ pathway for the Fe and Co motif, but not the Ni motif. Focussing entirely on Fe-based sites, Kattel *et al.* [193] used the same approach and functional as described above to investigate the ORR activity of Fe-N_x, $x = 2,4$ sites embedded in an infinite graphene plane. On the basis of formation energies, the Fe-N_4 was predicted to be more likely, although both types of site was found to support a one-site $4e^-$ ORR pathway. Pathway calculations (*i.e.* of both reaction intermediates and transition states, or rather saddle-points, between these intermediates) of the O_2 dissociation was investigated in terms of the spin dependence by Orellana [194], who considered the Me-N_4 site (Me=Fe, Mn and Co) embedded in an infinite graphene sheet as the dissociation site using PW-DFT PBE calculations. Based on these data, both the Fe- and Mn-based sites showed promise for ORR catalyst materials.

Szakacs *et al.* [189] applied periodic PBE calculations to predict the structures of model Fe/N/graphene catalysts, based on FeN_4 motifs embedded in graphene in a variety of geometries, including in an infinite graphene plane (see Fig 10), and located between two graphene nanoribbon edges. These authors also estimated the free energy of binding of key ORR intermediates (H_2O, O_2, OH, OOH, O) at the reactive FeN_4 site, and included an estimate of the free energy of solvation at the catalyst interface. On the basis of these findings, the catalyst materials were predicted to be active, and were supported by experimental data (Mössbauer spectroscopy). Adsorption of key ORR intermediates, and some of the key steps in the ORR pathway were calculated at the PBE level for a FeN_4 motif embedded in an infinite graphene sheet [195]. These authors predicted that the 2-electron pathway was disfavoured at the FeN_4 site, in accordance with other recent studies outlined above. Moving from consideration of isolated Fe-N_x ($x = 2,3,4$) sites in graphene, Holby *et al.* [196] probed the most likely structures for various *distributions* of these motifs, as embedded in the edges of graphene nanoribbon substrates, and the ORR activity of these multi-site catalyst materials. By calculation of the O_2 adsorption intermediate binding energies, the clustered bimetallic Fe-N_3 system was found to be the most promising compared with lone sites. These authors also used FPMD simulations to check that these clustered catalyst substrates were stable in the presence of liquid water.

With periodic PBE calculations, Sun *et al.* [197] considered

both 4- and 5-coordinated Fe/N sites embedded in an infinite graphene substrate, with a site concentration of ∼7 wt% (where experimentally-identified optimal concentrations span 0.02 to 2 wt%). While not explicitly considering the presence of liquid water at the interface, these authors employed a continuum solvation model based on a modification of the Poisson-Boltzmann equation, in combination with micro-solvation around the active site. These authors calculated adsorbed binding energies and transition states for parts of the ORR pathway, indicating that both types of sites can catalyse the ORR with good selectivity for the $4e^-$ pathway. In their recent study, Liang *et al.*[198] rightly noted that one difficulty in drawing clear conclusions from the previously reported calculations on Me/N/graphene systems is the lack of a unified computation scheme (*i.e.* different density functionals, PW or real-space DFT, *etc*), impeding a fair comparison between the different studies. To address this, these authors investigated fourteen different N- and Fe-N sites embedded in the basal plane and edges of graphene, using periodic PBE calculations in partnership with the COSMO[199] continuum solvation model. Their prediction of ORR intermediate binding energies was used to infer catalyst activity.

While Me-N-graphene sites have received a growing amount of attention in recent years, a considerable focus has been placed on predicting the structure of other types of dopant sites in graphene. By considering graphene ribbons of infinite length in their periodic PBE calculations, Huang *et al.*[201] analyzed the dopant-site dependence on the effect of nitrogen doping on electronic structure of the graphene. These authors also explored electronic effects of boron doping, in addition to quantifying the influence of more than one nitrogen, and finally, the presence of B and N co-dopants. Their results indicated that co-doping enabled favourable site location for the active nitrogen dopant. A localized spatial distribution of N-dopant sites was predicted by Feng *et al.*[202] to be stabilized by co-dopants such as B, Fe and Co. These localized 'N-clusters' (3 or 4 nitrogens in close spatial proximity) were found, via PW-DFT PW91 calculations, to enhance O_2 adsorption up to a level comparable with that on a Pt(111) surface, suggestive of good catalytic activity. A key finding of their calculations was that the co-dopants provided beneficial stabilization of the N-cluster in the CAC, while not compromising this indicator of cataltyic activity. In recogition of the fact that co-doping of N and B of graphene can be challenging from an experimental point of view, and in light of the propensity to form BN (which is catalytically inactive) in this instance, Liang *et al.*[203] used real-space B3LYP calculations on small graphene flakes ($C_{37}H_{15}$) to investigate the electronic structure of S and N co-doped graphene. These authors attempted to explain the experimentally-observed catalytic behaviour of these materials on the basis of calculated electron spin densities in the vicinity of the dopant sites.

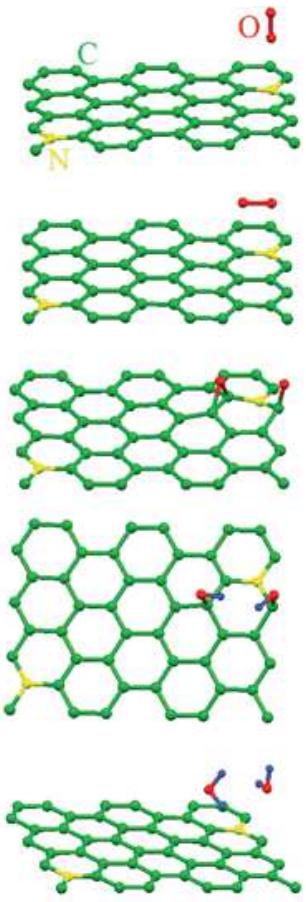

Fig. 11 Structures for five steps in the ORR from top to bottom on a 4% N-doped graphene substrate. Green, yellow, blue and red spheres are C, N, H and O respectively. Taken from Boukhvalov and Son[200].

A comprehensive and rigourous set of graphene dopant screening calculations (using PW-DFT with the Perdew functional) were reported by Kaukonen *et al.*[204], for both single and double doping sites. These authors targeted both the formation energy of the doped structure, and the O_2 adsorption energy, as their key metrics for evaluating the suitability of each candidate catalyst material. As dopants, the authors considered all first-row transition-metal atoms, plus the metals Al, Ru, Rh, Pd, Pt, Ga, Sn and Bi, and also the non-metals N, P, and B. On the basis of their criteria, the most viable catalyst materials were single-site dopants comprising Ni, Pd, Pt, Sn, and P.

Rani and Jindal[156] focussed entirely on predicting likely structure for co-doped B- N-graphene, by exploring effects of dopant concentration and dopant site spatial distribution. Their PW-DFT PBE calculations demonstrated the possibility for tuning the bandgap of these doped graphene materials,

based on symmetry considerations. As an example of a systematic process to identify doping structures, the use of cluster expansion theory[205,206] was reported by Seo *et al.*[183] to propose and screen, via PW-DFT PBE calculations, 117 different dopant site structures ranging from 0% to 100% doping levels of nitrogen in graphene. As an alternative to nitrogen and boron doping, Zhang *et al.*[207] explored the electronic effects of sulfur doping, using finite hydrogen-terminated graphene flakes (100 carbon atoms). By considering a range of dopant sites, their real-space B3LYP calculations revealed a preference for surface-adsorbed sulfur.

The influence of dopants on graphene surfaces with defects has been investigated by quantum chemical approaches[202,207–211]. In one recent report[210] a large part of their work was devoted to an exhaustive study of boron, nitrogen, and B/N co-dopants on the double-vacancy (555-777) graphene surface. Their data indicate that a dopant structure with three boron atoms and seven nitrogen atoms, at the centre of the defect, was the most favourable in terms of formation energy. Besides the Stone-Wales defect[212] and the divacancy defect, monovacancies are also common for graphene substrates. The effect of the oxidation of monovacancy sites on the N-doping of graphene was investigated by Hou *et al.*[213] using PW-DFT PBE calculations.

One limitation that of all DFT calculations, summarised above, is their reliance on generalised gradient approximation (GGA) functionals, which are well known to have serious deficiencies when describing non-covalent interactions[16–18]. When describing the key stages of the ORR, it is preferrable that non-covalent interactions are described reasonably, despite the fact that covalent bonds are also being formed and broken. The recent calculations of Kwak *et al.*[214] have have attempted to correct for these shortcomings. These authors made use of the Grimme empirical correction[215] along with the PBE functional (PBE+D2) in their PW-DFT based screening predictions. In this work, the energies of $\sim$900 different N-doped graphene configurations (from 0% to 57.1% nitrogen) were calculated, with the aim of providing guidelines for the knowledge-based design of ORR catalysts. These authors also calculated the Gibbs free energy for the intermediates of the ORR, for a given electrode potential. These results indicated that the catalytic efficiency of the ORR decreased as the dopant concentration increased, with better performance for bulk substituents over edge sites. In constrast to many existing studies, these authors also considered how the presence of liquid water at the graphene interface influenced the binding of the ORR intermediates. However, they found that stabilisation of adsorbed atomic oxygen was found to be the key determinant in the ORR, even in the presence of water molecules (approximating liquid water).

While quantum chemical calculations can predict a wide range of ideal dopant site structures, it is a different challenge to realise these structures in an experimental setting. Experimental determination of the structure of ORR-relevant sites on graphene and related compounds is pivotal to elucidating the fundamental structure-function relationships inherent to these catalytic materials. X-ray based techniques, such as X-ray photoelectron spectroscopy (XPS), X-ray emission spectroscopy (XES) and X-ray absorption spectroscopy (XAS) are the chief techniques for accomplishing this. Electronic structure theory calculations provide essential complementary data to enable assignment of site types with greater confidence. For example, Hou *et al.*[217] used a combination of XAS and periodic DFT (PBE) calculations of infinite graphene sheets, and finite graphene flakes and nanoribbons. On the basis of these calculations they could simulate C K-edge XAS spectra, with a focus on edge hydrogenation state. Since nitrogen dopants in graphene are a leading candidate material for ORR catalysts, the clear and unambiguous identification of types of nitrogen dopant structures in an experimental setting is a high priority. This is particularly true for distinguishing pyridinic and pyrollic nitrogen sites.

By comprehensively considering nitrogen doping in the vicinity of graphene nanoribbon edges, with differing edge hydrogenation states, Wang *et al.*[218] were able to identify the role of dihydrogenated carbons in stabilising nitrogen sites near the ribbon edges. From their periodic DFT calculations, they were also able to simulate XAS and XES spectra of N-doped graphene nanoribbons. However, these authors were unable to make unambiguous assignments of the nitrogen dopant sites in this work, although in a later study by some of the same authors[219], a more conclusive analysis was reached. The successful interpretation of XPS spectra relies on the use of reference spectra; this is problematic for nitrogen dopants in graphene, for which some reference spectra are not available. To address this problem with regards to ORR-relevant Me-N_x dopants (where Me is Fe, Co , *etc*), Artyushkova *et al.*[220] reported a methodical comparison of DFT-predicted N 1*s* binding energy shifts with reference XPS spectra, for the purposes of successfully identifying Me-N_4 *vs.* Me-N_2 sites *in-situ* in doped graphene. Aside from x-ray based techniques, where the characterisation of dopants is observed in a spatially *averaged* sense, scanning tunneling microscopy (STM) has been profitably used, in partnership with DFT calculations, to characterise *individual* nitrogen dopant sites in graphene[221].

Quantum chemical calculations have found widespread use in the prediction of the binding energies and structures of adsorption intermediates along the proposed ORR pathway, in the presence of CACs[200,207,209–211,223–225,228**?**], particularly nitrogen-doped CACs. Basing their studies on small ($C_{41}H_{17}$) graphene flakes doped with a nitrogen atom, Sidik *et al.*[222] used real-space B3LYP calculations with modest basis sets to predict partial charge distributions of the substrate, adsorption

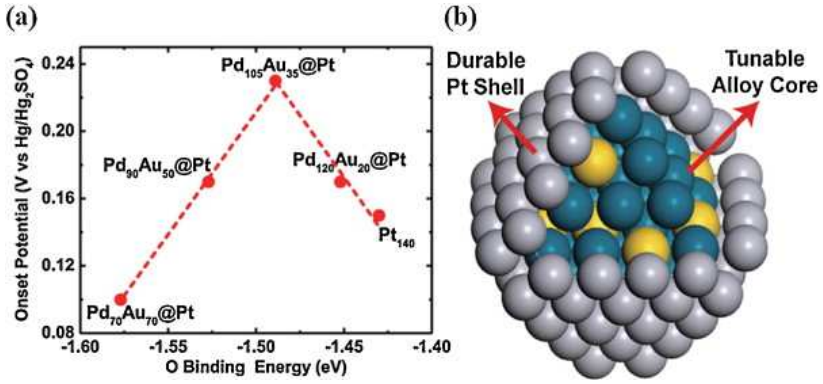

Fig. 12 a) Experimentally determined onset potential for the ORR at $Pd_xAu_{(1-x)}Pt$ core-shell nanoparticles, plotted as a function of the corresponding oxygen binding energy calculated by DFT. b) Illustrative structure of $Pd_xAu_{(1-x)}Pt$ core-shell nanoparticles. Reproduced with permission from Ref[216].

free energies of ORR intermediates, and reversible potentials for forming these intermediates. The predictions of the latter were in good agreement with experimental observations. These authors predicted that a $2e^-$ reduction pathway, with nitrogen dopant sites far from the sheet edges being the most active. Kurak and Anderson[223] built on this work by considering graphene nanoribbons with two nitrogen atoms placed on adjacent edge sites, using PW-DFT with the PW91 functional. Their predictions of the ORR-relevant reversible potentials indicated that $2e^-$ reduction to H_2O_2 was more likely than the desired $4e^-$ pathway.

Instead of edge dopant sites, Okamoto[224] considered nitrogen dopants in the basal plane of an infinite graphene sheet, via PW-DFT PBE calculations, where the number of dopant nitrogen atoms was varied. As one part of this study, Okamoto calculated the binding energy of O_2 and other intermediates adsorbed on these sites. After identifying a $4e^-$ pathway, reversible potentials for the intermediate steps of this pathway were predicted using these binding energies. This study raised the possibility of catalyst poisoning, at least for doped structures with higher nitrogen concentrations.

Using a similar approach to Sidik *et al.*[222], Zhang and Xia[225] also used graphene nanoflakes (46 carbon atoms) as a model substrate for studying the influence of a single nitrogen dopant atom on the binding of ORR-relevant intermediates, by applying B3LYP calculations with modest basis sets. However, unlike Sidik *et al.*[222], Zhang and Xia[225] considered edge sites. Their findings indicated that a catalysed $4e^-$ pathway was possible on these substrates. In a follow-up study on the same model substrate[209], calculations at the same level of theory focussed on how the number of nitrogen dopant sites and the presence of Stone-Wales defects influenced the binding energies of ORR intermediates. These authors found that higher concentrations of dopants were detrimental to predicated catalytic behaviour. With a focus on the adsorption energy and geometry of intermediate states along the ORR pathway (see Fig 11), Boukhvalov and Son[200] concluded from their periodic PBE calculations that a nitrogen dopant concentration of 4% (close to the experimentally reported value of 5%) allowed the initial stages of the ORR process (*e.g.* O_2 adsorption and dissociation) to proceed at a much lower energy cost compared with pristine graphene, while the energetics of the latter ORR stages were less influenced by doping.

Recently, quantum chemical studies on this topic have also considered the influence of other dopants on the binding of ORR intermediates. Having used PW-DFT PBE calculations to identify plausible sites in their study of boron-nitrogen co-dopants in graphene substrates with defects, Sen *et al.*[210] calculated adsorption energies of O_2 and related these to activated ORR processes. The presence of sulfur dopants in graphene and their impact on binding of ORR intermediates was explored by Zhang *et al.*[207]. The model substrate was a hydrogenated graphene nanoflake with 100 carbon atoms, and a range of sulfur dopant sites were investigated, with Stone-Wales defects also considered. As in a number of previous studies, real space B3LYP calculations with modest basis sets were used; the authors reported that both $2e^-$ and $4e^-$ ORR pathways were possible.

Zhang *et al.*[226] investigated the catalytic effect of silicon dopants in graphene, alongside the effects of interfacial curvature. Their periodic PBE calculations (based on both an infinite graphene plane and a (10,0) carbon nanotube) indicated that O_2 adsorption strength over the Si dopant site increased when going from a convex, to flat, to a concave surface, with the corresponding free energy change of the rate-determining step in the ORR becoming lower. Tuning of the ORR catalytic activity via manipulation of interfacial curvature was also the subject of a quantum chemical study reported by Chai

et al.[211], who considered nitrogen dopants in graphene sheets (both basal sites and edge sites) and (n,0) carbon nanotubes (where n =6–18). These authors also considered the presence of defects (mainly divacancy and Stone-Wales defects) in these doped structures. After applying FPMD to estimate the O_2 adsorption barrier in a liquid water environment as a means to identify promising candidate sites (using the HCTH functional[227], which unlike other GGAs, yields an excellent estimate of the O_2 binding energy and bond length), these authors used PW-DFT PBE calculations to predict free energies for the intermediates along the a number of possible ORR pathways, including the standard $4e^-$ ORR pathway. Their results indicated one particular site configuration that can approach the maximum ORR activity (for the standard pathway).

Rather than using hydrogenated graphene nanoflakes as replacement models for infinite graphene sheets, and motivated by experimental observations of ORR activity on N-doped graphene quantum dots (GQDs), Saidi reported DFT calculations on ten model N-doped, hydrogenated GQD structures ($\sim$40-50 carbon atoms), including graphitic and edge dopant sites. One key distinctive feature of this study was the use of vdW-DF functionals (for example Dion *et al.*[21], see Section 'Computational Methods'); another was the use of approximations to account for solvation effects, based on micro-solvation (with 2–6 water molecules). By calculating the binding free energies of the ORR intermediates, the author showed that both graphitic and pyridinic edge dopant sites conferred ORR catalytic activity.

As a combined experimental and theoretical study, and as part of a more comprehensive and broadly holistic approach to explaining ORR performance of existing doped CACs, and to theoretically predicting optimal ORR performance for new CAC materials, Jiao *et al.*[228] used real space B3LYP calculations with modest basis sets to calculate the free energies of intermediates in the ORR process. A continuum solvation model, PCM[229] was used to capture long-ranged solvation effects. Their calculations were based on small hydrogenated graphene nanoflakes, doped at a range of sites with N, B, P, S and O atoms. In addition, using a natural bond order[230] (NBO) analysis, these authors introduced a new activity descriptor for CACs, being the difference between the lowest valence orbital energy of the active centre and the highest valence orbital energy of the entire graphene cluster. This descriptor theoretically motivates an as-yet unknown dopant type, configuration and/or combination that yields an optimal ORR activity. In a related study regarding the hydrogen evolution reaction[231], this structural model and computational approach (same functional and basis set) were used to investigate dual-doped structures with N, B, O, S, P, F substituents.

Interestingly, going beyond free graphene as a catalysis substrate, and as a way to investigate the possible corrosion-resistant properties of graphene supported on transition-metal surfaces, Noh *et al.*[232] reported calculations of ORR reaction intermediates on both nitrogen-doped free graphene and supported graphene (on Cu(111), Ni(111) and Co(0001) surfaces). Their PW-DFT calculations included empirical dispersion corrections[215], and accounted for the presence of water at the molecular level. Their findings suggested that the Cu(111) support was the most promising for ORR activity.

A more thorough examination of the viability of graphene-based CACs for fuel cell applications has been made via the prediction of ORR pathways, as opposed to identification of intermediates only. In brief, two classes computational approaches have been applied in this context; first-principles molecular dynamics (FPMD) simulations, and, static geometry optimisation (including identification of transition state structures on the reaction pathway) using DFT calculations. Historically, both strategies have been reliant on the application of DFT, and both have strengths and weaknesses. In the FPMD approach, temperature effects can be accounted for, as can the dynamic representation of liquid water at the CAC interface. However, it is challenging to extract reaction barriers from the FPMD (*e.g.* via the Blue Moon ensemble[233,234], as reported in a number of previous studies[218,235,236] – *vide infra*), especially given the large error bars associated with these systems. Furthermore, the sheer system size and complexity becomes a limiting factor for FPMD, as this curtails the maximum possible duration of the trajectories used to extract this information. This also limits the degree of configurational sampling of the system, and therefore relevant mechanisms/pathways may be missed. On the other hand, static DFT calculations, while conducted at 0 K, can be approximately corrected for temperature effects. The range of possibilities of reaction pathways can be very thoroughly and systematically mapped out, particularly with reference to selectivity of the $2e^-$ reaction *vs.* the (preferred) $4e^-$ ORR process. Relatively larger system sizes can, in principle, be considered. However, the presence of water (at the molecular level of detail) at the CAC interface can only be addressed in a static manner, typically via microsolvation approaches. Regardless, it is imperative that any transition-states (TSs) found are also tested via calculation of reaction pathways, such that the TS can be clearly shown to connect two minima on the PES.

Ikeda *et al.*[236] doped graphene sheets with nitrogen both at the sheet edges and basal plane. Using the Car-Parrinello MD (CPMD)[237] approach in partnership with the Blue Moon ensemble, these authors calculated the free energy barriers for the adsorption and reduction of O_2 at these sites. They found that O_2 preferrentially adsorbed at carbon edge sites where a nitrogen dopant site was nearby. Okamoto[224] considered a model nitrogen-dopant configurations (with 1–4 nitrogens) as a structural model for subsequent FPMD simulations of O_2 adsorption and reaction, in the presence of liquid water. These PW-DFT PBE FPMD simulations were combined with

subsequence static DFT calculations to elucidate a $4e^-$ ORR pathway, and identify routes to the (unwanted) $2e^-$ reaction. Wang *et al.*[218] used CPMD with the Blue Moon ensemble to demonstrate how it was possible for O_2 to dissociatively attack the CH edge groups of N-doped graphene. Recently, Ikeda *et al.*[235] reported the use of CPMD with the Blue Moon ensemble to elucidate the ORR mechanism at graphene edges doped with nitrogen, and co-doped both with N and O atoms, and N and S atoms. Their resulting CPMD trajectories suggest that both grahphitic and pyridinic N-doping sites lead to activation of the $4e^-$ ORR process under acidic conditions, but via different mechanisms.

Alternatively, there are a number of studies on the static calculation of reaction pathways relavant to the ORR process at CAC interfaces. Based on a model graphene nanoflake structure (circumcoronene), Fazio *et al.*[238] used real-space B3LYP calculations with modest basis sets. Minima and true transition states (identified by diagonalisation of the Hessian matrix) were located on the ORR path for both associative and dissociative pathways, considering both the Eley-Rideal and Langmuir-Hinschelwood mechanisms. These authors also considered continuum solvation effects (PCM) and +D3 empirical dispersion corrections[239,240]. On the basis of their resulting free energy diagrams, these authors predicted the overpotentials required for spontaneous reaction under both acidic and basic conditions. While it is more common to see TS structure optimisations in the context of real-space DFT calculations, Kim *et al.*[241] used PW-DFT PBE calculations along with the nudged elastic band (NEB)[242] approach to predict reaction barriers for oxygen adsorption in *periodic* N-doped graphene systems. The presence of the dopants was found to reduce the oxygen adsorption barrier as well as the first electron transfer barrier.

Despite the considerable body of work summarised here, a substantial research effort using quantum chemical approaches clearly remains for future studies. Of particular interest from the point of view of reducing the amount of Pt in ORR catalyst materials are intermetallic core-shell nanocatalysts (IMCs)[216], see Fig 12. In addition to the significant complexities in synthesising these materials, as well as organising their stable arrangement on a graphene surface, there will also be challenges in modeling these catalysts – see Gracia-Espino *et al.*[243] for an example. Advances in synthetic strategies for shape-controlled catalytic metal NPs may also motivate more detailed quantum chemical studies of supported metal clusters in terms of predicting facet-specific reactivities for the ORR.

Lithium/Alkali Metal Batteries

Graphene has generated substantial interest as a material for possible use in lithium (or other alkali metal) ion batteries (LIBs). The setup of a typical LIB is shown in Fig. 13, with an anode and cathode made from layered materials into which the Li^+ ions can intercalate. Between the two is an Li^+ conducting electrolyte. When the device is charging the applied voltage causes the Li^+ ions to move from the cathode, through the electrolyte to the be intercalacted between the graphite layers of the anode. When the device is in use the Li^+ ions flow back the other way, and their is a flow of electrons from the anode to the cathode. The nature of the electrodes are one of the most important factors in LIBs, playing a crucial role in determining energy and power density, as well as battery lifetime.[244,245] One limiting factor of LIBs is the storage Li storage capacity of the graphite electrode, and graphene has been suggested as potential replacement, due to a possible higher storage capacity and reduced charging times.[244,246,247] Computational methods have played an important role in clarifying some of the properties of graphene as a potential electrode.

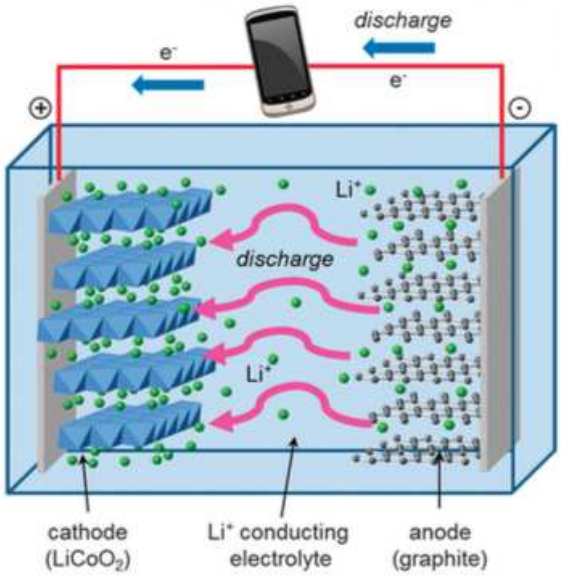

Fig. 13 Schematic of a first-generation rechargeable lithium-ion cell. During charging, lithium ions flow to the negative electrode through the electrolyte and electrons flow from the external circuit. During discharge the directions are reversed, generating useful power to be consumed by the device. Taken from Ref.[245]

Simulation studies in the area can be largely divided into two sets, MD simulations of electrolytes at graphene (see Section 'Simulations of Electrolytes at Graphene Interfaces'), and DFT calculations investigating the adsorption of the Li^+ to the graphene electrodes[247–259] which are discussed below.

The maximum Li capacity of graphite is 372 mA h/g, where Li^+ atoms are adsorbed as LiC_6 in a $(\sqrt{3}\times\sqrt{3})R30^\circ$ structure, with the Li^+ atoms located in the hollow sites.[23,246,247] Experimental studies have found that graphene systems are able to achieve specific capacities above 372 mA h/g.[244,246,247] Some

initial theoretical studies predicted that a sheet of graphene was able to exceed the maximum theoretical capacity of graphite due to the adsorption of Li atoms to both surfaces of the sheet, allowing a higher Li/C ratio than 1:6.[246,250,252,254] In particular, it has been predicted that a Li_2C_2 structure was theoretically stable,[250,251] with one Li ion adsorbing atop a carbon atom and another Li ion adsorbing above the C atom on the opposite side of the sheet, with the result of the graphene sheet buckling and forming a structure similar to that of graphane. However, more recent theoretical studies[247,260,261] (supported by Raman spectra that show that the intercalation of Li in few-layer graphene resembles that of graphite[262]) have suggested that that pristine graphene systems may have a theoretical Li^+ capacity that is lower than that of graphite. Using cluster expansion methods and DFT calculations, Lee and Persson found that the adsorption energy of Li to a single layer of graphene was positive for all Li coverages studied.[260] They assigned this apparent contradiction with previous theoretical studies that have found favourable adsorption energies[248–252,257] to the use of difference reference states. Lee and Persson defined the references states as pure single layer graphene and metallic Li, due to the fact that Li metal can form in Li-ion batteries, if a Li gas atom was used as a reference state then they found that a negative adsorption energy for some structures. Fan *et al.* further investigated if pristine graphene sheets could work through a kinetically limiting process by choosing a reference state as the adsorption of an adatom of Li to a Li(001) surface.[258] Under this condition they found that it was favourable for Li to adsorb to pristine graphene but only at concentrations lower than LiC_6.

One possible reason for the higher Li capacities observed in experiment may be due to the presence of defects in the graphene sheets.[247,255,261,263] Fan *et al.* found that vacancy defects present in a graphene sheet are both able to increase the Li/C ratio and enhance the diffusion energetics of Li^+.[247] Zhou *et al.* have predicted that both divacancy and Stone-Wales defects are energetically favourable sites for Li adsorption and could enhance Li adsorption on graphene.[255] In addition, the same authors also predicted that Li adsorption at graphene grain boundaries was favourable with respect to bulk Li.[263] These calculations also found that energy barrier to diffusion along the grain boundary was lower than that perpendicular to the boundary suggesting that grain boundaries may be able to act as channels for Li atoms. Uthaisar and Barone investigated the diffusion pathways of Li close to the edge of graphene nano-ribbons, and also found that diffusion was faster close to the edge than along the bulk surface.[264] Wigner V_2^2 defects in multilayer graphene have also been found to be energetically favourable for Li adsorption compared with pristine graphene[256] Defects have also been predicted to support the adsorption of Na^+ and Ca^{2+} ions to graphene surfaces.[259] On pristine graphene surfaces neither metal is able to absorb, however, with a sufficient density of defects a capacity higher than that of bulk graphite can be achieved. The predictions of computational studies that the presence of defects can improve the performance of LIBs has been supported by recent experimental evidence. By tailoring the nanostructure of the graphene sheet the Li^+ storage capacity can be increased.[265,266]

Another possibility of increasing the storage capacity of graphene for use in LIBs is to dope the graphene with other elements, typically boron or nitrogen[261,267–272] Lui *et al.* found that substituting a B atom for an C atom, thus creating a slightly electron deficient system, promoted the adsorption of Li compared with pristine graphene. In contrast, replacing a C atom with N was unfavourable. Experimental studies have also found that doping graphene with N or B can improve the reversible capacity of the system, as well as improving the charging/discharging times.[273,274] Other studies have investigated the effect of graphitic (where a C atom is substituted for a N atom), pyridinic and pyrrolic N (where in addition to the substitution C atoms are removed) doping.[267,268] While graphitic N-doped graphene is more unfavourable for Li adsorption than pristine graphene, pyridinic and, to a lesser extent, pyrrolic N-doped graphene promotes the adsorption of Li, with the Li atom adsorbing in the centre of the defect site, as shown in Fig. 6. Hardikar *et al.* investigated both the storage capacity and energy barriers to Li diffusion for a variety of defective, doped and doped defective graphene systems.[272] While a number of N-doped systems showed low energy barriers overall they concluded that B doped monovacancy graphene was the most promising candidate. Boron doped graphene has also been shown allow the stable adsorption of Na^+ ions, significantly reducing the adsorption energy.[270]

Finally it should also be mentioned that other 2D carbon nanostructure, such as graphyne[269,275,276] and graphidyne[276,277] have been investigated theoretically as possible anode materials molecules, with the B-doped graphyne significantly outperforming pristine graphyne.[269]

Summary and Outlook

Computational methods have advanced a long way in the last decade but there are still a number of challenges that have to be met. Fig. 14 shows, schematically, the challenges that need to be overcome for the different computational approaches as well as the developments that are required for progress. These challenges and developments are outlined in more detail below.

The continuing increases in computational power mean that MD and MC simulations of greater time- and length-scales will be possible in future. However, merely simulating larger systems for longer durations will not necessarily provide more

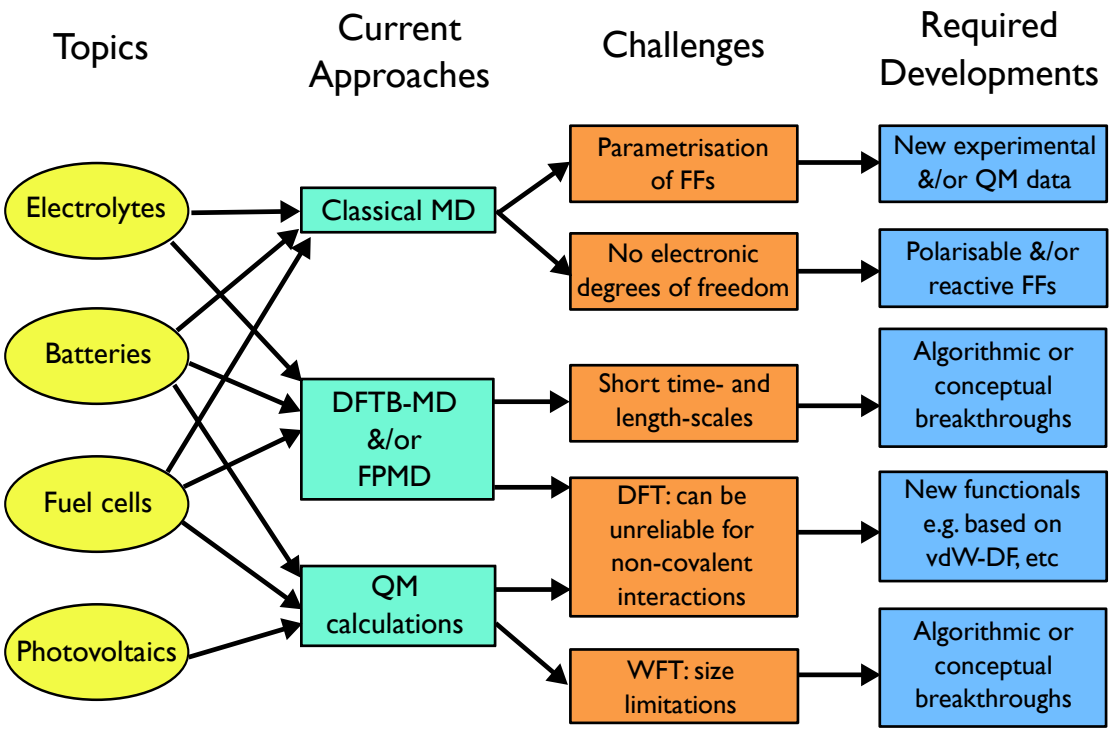

Fig. 14 Schematic diagram of the challenges for the current computational approaches discussed in this review, as well as the developments required for progress.

insight unless the advances in computing power are accompanied by corresponding advances in simulation techniques and methodology.

One area of development for atomistic simulations of graphene-based energy materials is in the refinement of force-fields (FFs). Parametrisation and validation of FFs, particularly for describing complex interfacial systems, remains an ongoing challenge. High-quality experimental and/or QM data is needed to ensure that the FFs used to model graphene-based materials are appropriate. The advances in QM, summarised in this Review, will continue to provide valuable input into the (re-)parametrisation of such FFs. The relatively greater cost that polarisable FFs generally incur is increasingly becoming less of a issue. This means that the development and use of polarisable FFs, especially for a highly conductive system such as graphene, is likely to play a major role in MD and MC simulations of graphene-based energy materials in future.

For example, in the MD simulations of electrolytes at graphene interfaces, polarisation may play a significant role; further studies systematically investigating these polarisation effects are certainly warranted. Such developments will ensure that MD simulations continue to play an important role in elucidating the structure of the graphene-electrolyte interface, as present in energy storage materials. The use of reactive FFs is also likely to increase over the next decade, although in this instance the challenge of parametrising such FFs remains a challenge. However, the ability to bridge the gap between QM and classical descriptions makes the development of reactive FFs an attractive prospect. Aside from FF development, the various techniques for improving the sampling of the potential energy surface have become increasingly commonplace over the last decade, and such methods are likely to find wider use in the energy materials space in future. The availability of meta-dynamics, umbrella sampling, steered MD and other such approaches means that calculation of free energy differences is now not unusual, often allowing a more direct comparison between simulation and experimental data.

Approaches based on quantum chemistry also face challenges in describing graphene-based energy materials. Modelling at the first-principles level of these systems has, by necessity, been accomplished using DFT. However, the inability of generalised gradient approximation (GGA) functionals to capture weak, non-covalent interactions is well-known. Unfortunately the bulk of the calculations published to date in this area have made use of such GGAs. A small number of studies have reported the use of the '+D' type empirical correction to DFT GGA functionals. However, this strategy is also not without limitation, in particular due to the transferrability of the parametrisation of the damping function that is associated with the dispersion correction. These damping functions have

typically been devised for intra- and inter-*molecular* interactions[278], not molecule–surface interactions. Further validation and/or refitting of these damping functions may be warranted. There are very few examples of quantum chemical calculations in the area of graphene-based energy materials that use vdW-DF functionals. While also not perfect, these functionals show substantial promise. Developments of this class of functional may be very beneficial for advancing graphene-based energy materials. In terms of first principles molecular simulation (FPMD) that are capable of describing dynamic bond breaking and bond formation events, there is a limited but growing number of studies appearing in this area. These may also form a valuable platform for cretating and validating new, more sophisticated force-fields. These advances in sampling techniques, force-field development and the possibilities of improved density functionals all give cause for expecting a very bright future for their application to graphene-based energy materials.

Acknowledgements

We thank the National Computing Infrastructure (NCI) for provision of computational resources. ZEH and TRW thank **veski** for research funding, and TRW thanks **veski** for an Innovation Fellowship.

References

1 K. S. Novoselov, A. K. Geim, S. V. Morozov, D. Jiang, Y. Zhang, S. V. Dubonos, I. V. Grigorieva and A. A. Firsov, *Science*, 2004, **306**, 666–669.
2 J. Liu, Y. Xue, M. Zhang and L. Dai, *MRS Bull.*, 2012, **37**, 1265–1272.
3 J. Zhang, F. Zhao, Z. Zhang, N. Chen and L. Qu, *Nanoscale*, 2013, **5**, 3112–3126.
4 M. P. Allen and D. J. Tildesley, *Computer Simulation of Liquids*, Oxford University Press, 1st edn, 1987.
5 D. Frenkel and S. B, *Understanding Molecular Simulation*, Elsevier, 2nd edn, 2002.
6 D. J. Wales and J. P. K. Doye, *J. Phys. Chem. A*, 1997, **101**, 5111–5116.
7 Z. Li and H. A. Scheraga, *Proc. Natl. Acad. Sci. U.S.A*, 1987, **84**, 6611–6615.
8 Z. E. Hughes, S. M. Tomásio and T. R. Walsh, *Nanoscale*, 2014, **6**, 5438–5448.
9 N. Metropolis, A. W. Rosenbluth, M. N. Rosenbluth, A. H. Teller and E. Teller, *J. Chem. Phys.*, 1953, **21**, 1087–1092.
10 G. M. Torrie and J. P. Valleau, *J. Comput. Phys.*, 1977, **23**, 187–199.
11 C. Jarzynski, *Phys. Rev. Lett.*, 1997, **78**, 2690.
12 A. Laio, *Proc. Natl. Acad. Sci. USA*, 2002, **99**, 12562–12566.
13 A. Barducci, G. Bussi and M. Parrinello, *Phys. Rev. Lett.*, 2008, **100**, 020603.
14 A. Pohorille, C. Jarzynski and C. Chipot, *J. Phys. Chem. B*, 2010, **114**, 10235–10253.
15 Y. Zhang and W. Yang, *Phys. Rev. Lett.*, 1998, **80**, 890.
16 D. J. Lacks and R. G. Gordon, *Phys. Rev. A*, 1993, **47**, 4681.
17 T. van Mourik and R. J. Gdanitz, *J. Chem. Phys.*, 2002, **116**, 9620.
18 T. R. Walsh, *Phys. Chem. Chem. Phys*, 2005, **7**, 443–451.
19 J. Klimeš and A. Michaelides, *J. Chem. Phys.*, 2012, **137**, 120901.
20 S. Grimme, *J. Comput. Chem.*, 2004, **25**, 1463–1473.
21 M. Dion, H. Rydberg, E. Schröder, D. C. Langreth and B. I. Lundqvist, *Phys. Rev. Lett.*, 2004, **92**, 246401.
22 J. Klimeš, D. R. Bowler and A. Michaelides, *J. Phys.: Condens. Matter*, 2010, **22**, 022201.
23 Z. Wang, S. M. Selbach and T. Grande, *RSC Adv.*, 2014, **4**, 4069–4079.
24 J. P. Perdew, A. Ruzsinszky, G. I. Csonka, O. A. Vydrov, G. E. Scuseria, L. A. Constantin, X. Zhou and K. Burke, *Phys. Rev. Lett.*, 2008, **100**, 136406.
25 É. D. Murray, K. Lee and D. C. Langreth, *J. Chem. Theory Comput.*, 2009, **5**, 2754–2762.
26 K. Lee, É. D. Murray, L. Kong, B. I. Lundqvist and D. C. Langreth, *Phys. Rev. B*, 2010, **82**, 081101.
27 K. Berland and P. Hyldgaard, *Phys. Rev. B*, 2013, **87**, 205421.
28 M. Rubeš, J. Kysilka, P. Nachtigall and O. Bludský, *Phys. Chem. Chem. Phys.*, 2010, **12**, 6438–6444.
29 P. Lazar, F. Karlický, P. Jurečka, M. Kocman, E. Otyepková, K. Šafářová and M. Otyepka, *J. Am. Chem. Soc.*, 2013, **135**, 6372–6377.
30 R. Zacharia, H. Ulbricht and T. Hertel, *Phys. Rev. B*, 2004, **69**, 155406.
31 O. Bludský, M. Rubeš, P. Soldan and P. Nachtigall, *J. Chem. Phys.*, 2008, **128**, 114102.
32 A. J. Misquitta and K. Szalewicz, *Chem. Phys. Lett.*, 2002, **357**, 301–306.
33 A. Heßelmann, G. Jansen and M. Schtz, *J. Chem. Phys.*, 2005, **122**, 014103.
34 G. R. Jenness and K. D. Jordan, *J. Phys. Chem. C*, 2009, **113**, 10242–10248.
35 G. R. Jenness, O. Karalti and K. D. Jordan, *Phys. Chem. Chem. Phys.*, 2010, **12**, 6375.
36 J. Kysilka, M. Rubeš, L. Grajciar, P. Nachtigall and O. Bludský, *J. Phys. Chem. A*, 2011, **115**, 11387–11393.
37 Y. Cho, S. K. Min, J. Yun, W. Y. Kim, A. Tkatchenko and K. S. Kim, *J. Chem. Theory Comput.*, 2013, **9**, 2090–2096.
38 P. Ganesh, J. Kim, C. Park, M. Yoon, F. A. Reboredo and P. R. C. Kent, *J. Chem. Theory Comput.*, 2014, **10**, 5318–5323.
39 R. Car and M. Parrinello, *Phys. Rev. Lett.*, 1985, **55**, 2471–2474.
40 T. D. Kuehne, M. Krack, F. R. Mohamed and M. Parrinello, *Phys. Rev. Lett.*, 2007, **98**, 066401.
41 G. Cicero, J. C. Grossman, E. Schwegler, F. Gygi and G. Galli, *J. Am. Chem. Soc.*, 2008, **130**, 1871–1878.
42 M. K. Rana and A. Chandra, *J. Chem. Phys.*, 2013, **138**, 204702.
43 C. Calero, J. Marti, E. Guardia and M. Masia, *J. Chem. Theory Comput.*, 2013, **9**, 5070–5075.
44 W. Zhang, P. Wu, Z. Li and J. Yang, *J. Phys. Chem. C*, 2011, **115**, 17782–17787.
45 Y. Wang, A. J. Page, Y. Nishimoto, H.-J. Qian, K. Morokuma and S. Irle, *J. Am. Chem. Soc.*, 2011, **133**, 18837–18842.
46 H.-B. Li, A. J. Page, C. Hettich, B. Aradi, C. Kohler, T. Frauenheim, S. Irle and K. Morokuma, *Chem. Sci.*, 2014, **5**, 3493–3500.
47 R. A. Nistor, D. M. Newns and G. J. Martyna, *ACS Nano*, 2011, **5**, 3096–3103.
48 R. A. Nistor, M. A. Kuroda, A. A. Maarouf and G. J. Martyna, *Phys. Rev. B*, 2012, **86**, 041409.
49 D. Porezag, T. Frauenheim, T. Köhler, G. Seifert and R. Kaschner, *Phys. Rev. B*, 1995, **51**, 12947.
50 M. Elstner, D. Porezag, G. Jungnickel, J. Elsner, M. Haugk, T. Frauenheim, S. Suhai and G. Seifert, *Phys. Rev. B*, 1998, **58**, 7260–7268.
51 W. Song, M. G. Jiao, K. Li, Y. Wang and Z. J. Wu, *Chem. Phys. Lett.*, 2013, **588**, 203–207.
52 R. X. Song, W. Feng, C. A. Jimenez-Cruz, B. Wang, W. R. Jiang, Z. G. Wang and R. H. Zhou, *RSC Adv.*, 2015, **5**, 274–280.

53 R. X. Song, S. Wangmo, M. S. Xin, Y. Meng, P. Huai, Z. G. Wang and R. Q. Zhang, *Nanoscale*, 2013, **5**, 6767–6772.
54 F. Iori and S. Corni, *J. Comput. Chem.*, 2008, **29**, 1656–1666.
55 A. W. Dick and B. G. Overhauser, *Phys. Rev.*, 1958, **112**, 90–103.
56 P. Ren and J. W. Ponder, *J. Comput. Chem.*, 2002, **23**, 1497–1506.
57 J. W. Ponder and D. A. Case, *Adv. Protein Chem.*, 2003, **66**, 27–85.
58 P. Ren and J. W. Ponder, *J. Phys. Chem. B*, 2003, **107**, 5933–5947.
59 T. R. Walsh, *Mol. Phys.*, 2008, **106**, 1613–1619.
60 A. J. Stone, *Chem. Phys. Lett.*, 1981, **83**, 233–239.
61 A. J. Stone and M. Alderton, *Mol. Phys.*, 1985, **56**, 1047–1064.
62 T. Liang, Y. K. Shin, Y.-T. Cheng, D. E. Yilmaz, K. G. Vishnu, O. Verners, C. Zou, S. R. Phillpot, S. B. Sinnott and A. C. T. van Duin, *Annu. Rev. Mater. Res.*, 2013, **43**, 109–129.
63 Y. K. Shin, T.-R. Shan, T. Liang, M. J. Noordhoek, S. B. Sinnott, A. C. T. van Duin and S. R. Phillpot, *MRS Bull.*, 2012, **37**, 504–512.
64 A. van Duin, S. Dasgupta, F. Lorant and W. A. Goddard, *J. Phys. Chem. A*, 2001, **105**, 9396–9409.
65 C. Zhang, Y. Wen and X. Xue, *ACS Appl Mater Interfaces*, 2014, **6**, 12235–12244.
66 S. Goverapet Srinivasan and A. C. T. van Duin, *J. Phys. Chem. A*, 2011, **115**, 13269–13280.
67 T. Liang, T.-R. Shan, Y.-T. Cheng, B. D. Devine, M. Noordhoek, Y. Li, Z. Lu, S. R. Phillpot and S. B. Sinnott, *Materials Science & Engineering R*, 2013, **74**, 255–279.
68 T. P. C. Klaver, S.-E. Zhu, M. H. F. Sluiter and G. C. A. M. Janssen, *Carbon*, 2014, 1–10.
69 M. C. Gordillo and J. Mart, *J. Chem. Phys.*, 2002, **117**, 3425.
70 A. Pertsin and M. Grunze, *J. Phys. Chem. B*, 2004, **108**, 1357–1364.
71 R. L. Jaffe, P. Gonnet, T. Werder, J. H. Walther and P. Koumoutsakos, *Mol. Simul.*, 2004, **30**, 205–216.
72 M. C. Gordillo, G. Nagy and J. Martí, *J. Chem. Phys.*, 2005, **123**, 054707.
73 J. Martí, G. Nagy, M. C. Gordillo and E. Guardia, *J. Chem. Phys.*, 2006, **124**, 094703.
74 A. Pertsin and M. Grunze, *J. Chem. Phys.*, 2006, **125**, 114707.
75 G. R. Birkett and D. D. Do, *J. Phys. Chem. C*, 2007, **111**, 5735–5742.
76 M. Gordillo and J. Martí, *Phys. Rev. B*, 2008, **78**, 075432.
77 J. Sala, E. Guardia and J. Martí, *Phys. Chem. Chem. Phys.*, 2012, **14**, 10799.
78 C. Calero, M. C. Gordillo and J. Martí, *J. Chem. Phys.*, 2013, **138**, 214702.
79 T. A. Ho and A. Striolo, *J. Chem. Phys.*, 2013, **138**, 054117.
80 D. Konatham, J. Yu, T. A. Ho and A. Striolo, *Langmuir*, 2013, **29**, 11884–11897.
81 F. Taherian, V. Marcon and N. F. A. van der Vegt, *Langmuir*, 2013, **29**, 1457–1465.
82 Y. Wu and N. R. Aluru, *J. Phys. Chem. B*, 2013, **117**, 8802–8813.
83 X. Zhao and J. K. Johnson, *Mol. Simul.*, 2005, **31**, 1–10.
84 F. Moulin, M. Devel and S. Picaud, *Phys. Rev. B*, 2005, **71**, 165401.
85 S. M. Tomásio and T. R. Walsh, *J. Phys. Chem. C*, 2009, **113**, 8778–8785.
86 P. Schyman and W. L. Jorgensen, *J. Phys. Chem. Lett.*, 2013, **4**, 468–474.
87 W. L. Jorgensen, J. Chandrasekhar, J. D. Madura, R. W. Impey and M. L. Klein, *J. Chem. Phys.*, 1983, **79**, 926–935.
88 M. V. Fedorov and A. A. Kornyshev, *Chem. Rev.*, 2014, **114**, 2978–3036.
89 R. Burt, G. Birkett and X. S. Zhao, *Phys. Chem. Chem. Phys.*, 2014, **16**, 6519–6538.
90 S. A. Kislenko, I. S. Samoylov and R. H. Amirov, *Phys. Chem. Chem. Phys.*, 2009, **11**, 5584.
91 J. Vatamanu, O. Borodin and G. D. Smith, *J. Am. Chem. Soc.*, 2010, **132**, 14825–14833.
92 Y. Shim, H. J. Kim and Y. Jung, *Faraday Discuss.*, 2011, **154**, 249–263.
93 J. Vatamanu, L. Cao, O. Borodin, D. Bedrov and G. D. Smith, *J. Phys. Chem. Lett.*, 2011, **2**, 2267–2272.
94 M. V. Fedorov and R. M. Lynden-Bell, *Phys. Chem. Chem. Phys.*, 2012, **14**, 2552.
95 E. Paek, A. J. Pak and G. S. Hwang, *Journal of the Electrochemical Society*, 2012, **160**, A1–A10.
96 J. Vatamanu, O. Borodin, D. Bedrov and G. D. Smith, *J. Phys. Chem. C*, 2012, **116**, 7940–7951.
97 L. Xing, J. Vatamanu, O. Borodin, G. D. Smith and D. Bedrov, *J. Phys. Chem. C*, 2012, **116**, 23871–23881.
98 L. Xing, J. Vatamanu, G. D. Smith and D. Bedrov, *J. Phys. Chem. Lett.*, 2012, **3**, 1124–1129.
99 H. Zhou, M. Rouha, G. Feng, S. S. Lee, H. Docherty, P. Fenter, P. T. Cummings, P. F. Fulvio, S. Dai, J. McDonough, V. Presser and Y. Gogotsi, *ACS Nano*, 2012, **6**, 9818–9827.
100 Y.-L. Wang, A. Laaksonen and Z.-Y. Lu, *Phys. Chem. Chem. Phys.*, 2013, **15**, 13559–13569.
101 A. D. DeYoung, S.-W. Park, N. R. Dhumal, Y. Shim, Y. Jung and H. J. Kim, *J. Phys. Chem. C*, 2014, **118**, 18472–18480.
102 S. Kerisit, B. Schwenzer and M. Vijayakumar, *J. Phys. Chem. Lett.*, 2014, **5**, 2330–2334.
103 T. Méndez-Morales, J. Carrete, M. Pérez-Rodríguez, Ó. Cabeza, L. J. Gallego, R. M. Lynden-Bell and L. M. Varela, *Phys. Chem. Chem. Phys.*, 2014, **16**, 13271–13278.
104 J. Vatamanu, L. Xing, W. Li and D. Bedrov, *Phys. Chem. Chem. Phys.*, 2014, **16**, 5174–5182.
105 R. M. Lynden-Bell, A. I. Frolov and M. V. Fedorov, *Phys. Chem. Chem. Phys.*, 2012, **14**, 2693–2701.
106 O. Borodin, *J. Phys. Chem. B*, 2009, **113**, 11463–11478.
107 D. Bedrov, O. Borodin, Z. Li and G. D. Smith, *J. Phys. Chem. B*, 2010, **114**, 4984–4997.
108 Y. Shim, Y. Jung and H. J. Kim, *J. Phys. Chem. C*, 2011, **115**, 23574–23583.
109 K. Tasaki, *J. Phys. Chem. B*, 2005, **109**, 2920–2933.
110 I. A. Hamad, M. A. Novotny, D. O. Wipf and P. A. Rikvold, *Phys. Chem. Chem. Phys.*, 2010, **12**, 2740.
111 J. Vatamanu, O. Borodin and G. D. Smith, *J. Phys. Chem. C*, 2012, **116**, 1114–1121.
112 R. Jorn, R. Kumar, D. P. Abraham and G. A. Voth, *J. Phys. Chem. C*, 2013, **117**, 3747–3761.
113 K. Tasaki, A. Goldberg, J.-J. Lian, M. Walker, A. Timmons and S. J. Harris, *J. Electrochem. Soc.*, 2009, **156**, A1019.
114 K. Leung and J. L. Budzien, *Phys. Chem. Chem. Phys.*, 2010, **12**, 6583.
115 K. Leung, *J. Phys. Chem. C*, 2013, **117**, 1539–1547.
116 D. S. L. Abergel, V. Apalkov, J. Berashevich, K. Ziegler and T. Chakraborty, *Adv. Phys.*, 2010, **59**, 261–482.
117 D. W. Chang, H.-J. Choi, A. Filer and J.-B. Baek, *J. Mater. Chem. A*, 2014, **2**, 12136–12149.
118 A. Kasry, M. A. Kuroda, G. J. Martyna, G. S. Tulevski and A. A. Bol, *ACS Nano*, 2010, **4**, 3839–3844.
119 A. Du and S. C. Smith, *J. Phys. Chem. Lett.*, 2011, **2**, 73–80.
120 M. A. Kuroda, J. Tersoff and G. J. Martyna, *Phys. Rev. Lett.*, 2011, **106**, 116804.
121 M. A. Kuroda, J. Tersoff, D. M. Newns and G. J. Martyna, *Nano Lett.*, 2011, **11**, 3629–3633.
122 T. Hu and I. C. Gerber, *J. Phys. Chem. C*, 2013, **117**, 2411–2420.
123 S. Ryu, L. Liu, S. Berciaud, Y.-J. Yu, H. Liu, P. Kim, G. W. Flynn and L. E. Brus, *Nano Lett.*, 2010, **10**, 4944–4951.
124 Y. Yang and R. Murali, *Appl. Phys. Lett.*, 2011, **98**, 093116.
125 G. Giovannetti, P. Khomyakov, G. Brocks, P. Kelly and J. van den Brink, *Phys. Rev. B*, 2007, **76**, 073103.
126 A. Mattausch and O. Pankratov, *Phys. Rev. Lett.*, 2007, **99**, 076802.

127 F. Varchon, R. Feng, J. Hass, X. Li, B. Nguyen, C. Naud, P. Mallet, J. Y. Veuillen, C. Berger, E. Conrad and L. Magaud, *Phys. Rev. Lett.*, 2007, **99**, 126805.

128 S. Y. Zhou, G. H. Gweon, A. V. Fedorov, P. N. First, W. A. de Heer, D. H. Lee, F. Guinea, A. H. Castro Neto and A. Lanzara, *Nature Materials*, 2007, **6**, 770–775.

129 Y.-J. Kang, J. Kang and K. Chang, *Phys. Rev. B*, 2008, **78**, 115404.

130 G. Giovannetti, P. Khomyakov, G. Brocks, V. Karpan, J. van den Brink and P. Kelly, *Phys. Rev. Lett.*, 2008, **101**, 026803.

131 P. A. Khomyakov, G. Giovannetti, P. C. Rusu, G. Brocks, J. van den Brink and P. J. Kelly, *Phys. Rev. B*, 2009, **79**, 195425.

132 P. Shemella and S. K. Nayak, *Appl. Phys. Lett.*, 2009, **94**, 032101.

133 T. C. Nguyen, M. Otani and S. Okada, *Phys. Rev. Lett.*, 2011, **106**, 106801.

134 A. K. Manna and S. K. Pati, *Chem. Asian J.*, 2009, **4**, 855–860.

135 Y. H. Lu, W. Chen, Y. P. Feng and P. M. He, *J. Phys. Chem. B*, 2009, **113**, 2–5.

136 J. T. Sun, Y. H. Lu, W. Chen, Y. P. Feng and A. T. S. Wee, *Phys. Rev. B*, 2010, **81**, 155403.

137 M. Chi and Y.-P. Zhao, *Computational Materials Science*, 2012, **56**, 79–84.

138 J. P. Trinastic and H.-P. Cheng, *Phys. Rev. B*, 2014, **89**, 245447.

139 L. S. Panchakarla, K. S. Subrahmanyam, S. K. Saha, A. Govindaraj, H. R. Krishnamurthy, U. V. Waghmare and C. N. R. Rao, *Adv. Mater.*, 2009, 4726–4730.

140 N. Al-Aqtash, K. M. Al-Tarawneh, T. Tawalbeh and I. Vasiliev, *J. Appl. Phys.*, 2012, **112**, 034304.

141 C. L. Muhich, J. Y. Westcott IV, T. C. Morris, A. W. Weimer and C. B. Musgrave, *J. Phys. Chem. C*, 2013, **117**, 10523–10535.

142 X. Wang, Q. Cai, G. Zhuang, X. Zhong, D. Mei, X. Li and J. Wang, *Phys. Chem. Chem. Phys.*, 2014, **16**, 20749–20754.

143 S. Kim, J. Ihm, H. J. Choi and Y.-W. Son, *Phys. Rev. Lett.*, 2008, **100**, 146801.

144 T. Jayasekera, B. D. Kong, K. W. Kim and M. B. Nardelli, *Phys. Rev. Lett.*, 2010, **104**, 176802.

145 U. Starke, S. Forti, K. V. Emtsev and C. Coletti, *MRS Bull.*, 2012, **37**, 1177–1186.

146 H. Matsui, F. Matsui, N. Maejima, T. Matsushita, T. Okamoto, A. N. Hattori, Y. Sano, K. Yamauchi and H. Daimon, *Surface Science*, 2015, **632**, 98–102.

147 S. Tang, J. Yu and L. Liu, *Phys. Chem. Chem. Phys.*, 2013, **15**, 5067.

148 C. Stampfer, F. Molitor, D. Graf, K. Ensslin, A. Jungen, C. Hierold and L. Wirtz, *Appl. Phys. Lett.*, 2007, **91**, 241907.

149 H. E. Romero, N. Shen, P. Joshi, H. R. Gutierrez, S. A. Tadigadapa, J. O. Sofo and P. C. Eklund, *ACS Nano*, 2008, **2**, 2037–2044.

150 L. Liu and Z. Shen, *Appl. Phys. Lett.*, 2009, **95**, 252104.

151 J. Sławińska, I. Zasada and Z. Klusek, *Phys. Rev. B*, 2010, **81**, 155433.

152 Y. Fan, M. Zhao, Z. Wang, X. Zhang and H. Zhang, *Appl. Phys. Lett.*, 2011, **98**, 083103.

153 N. Kharche and S. K. Nayak, *Nano Lett.*, 2011, **11**, 5274–5278.

154 E. Kan, H. Ren, F. Wu, Z. Li, R. Lu, C. Xiao, K. Deng and J. Yang, *J. Phys. Chem. C*, 2012, **116**, 3142–3146.

155 T. Holme, Y. Zhou, R. Pasquarelli and R. O'Hayre, *Phys. Chem. Chem. Phys.*, 2010, **12**, 9461–9468.

156 P. Rani and V. K. Jindal, *RSC Adv.*, 2013, **3**, 802–812.

157 C. N. R. Rao and R. Voggu, *Materials Today*, 2010, **13**, 34.

158 Y.-H. Zhang, K.-G. Zhou, K.-F. Xie, J. Zeng, H.-L. Zhang and Y. Peng, *Nanotechnology*, 2010, **21**, 065201.

159 T. Yumura, K. Kimura, H. Kobayashi, R. Tanaka, N. Okumura and T. Yamabe, *Phys. Chem. Chem. Phys.*, 2009, **11**, 8275–8284.

160 U. S. D. of Energy, *Technical Plan Fuel Cells,*, United states deparment of energy technical report, 2012.

161 C. T. Campbell, S. C. Parker and D. E. Starr, *Science*, 2002, **298**, 811–814.

162 A. D. Becke, *J. Chem. Phys.*, 1993, **98**, 5648–5652.

163 P. Hohenberg and W. Kohn, *Phys. Rev.*, 1964, **136**, B864–B871.

164 S. H. Vosko, L. Wilk and M. Nusair, *Can. J. Phys.*, 1980, 1200–1211.

165 J. P. Perdew, J. A. Chevary, S. H. Vosko, K. A. Jackson, M. R. Pederson, D. J. Singh and C. Fiolhais, *Phys. Rev. B*, 1992, **46**, 6671–6687.

166 G. J. Soldano, P. Quaino, E. Santos and W. Schmickler, *J. Phys. Chem. C*, 2013, **117**, 19239–19244.

167 B. B. Xiao, X. Y. Lang and Q. Jiang, *RSC Adv.*, 2014, **4**, 28400–28408.

168 W. Qian, R. Hao, J. Zhou, M. Eastman, B. A. Manhat, Q. Sun, A. M. Goforth and J. Jiao, *Carbon*, 2013, **52**, 595–604.

169 J. P. Perdew, K. Burke and M. Ernzerhof, *Phys. Rev. Lett.*, 1996, **77**, 3865–3868.

170 P. Xu, L. Dong, M. Neek-Amal, M. L. Ackerman, J. Yu, S. D. Barber, J. K. Schoelz, D. Qi, F. Xu, P. M. Thibado and F. M. Peeters, *ACS Nano*, 2014, **8**, 2697–2703.

171 E. Gracia-Espino, G. Hu, A. Shchukarev and T. Wågberg, *J. Am. Chem. Soc.*, 2014, **136**, 6626–6633.

172 J. K. Nørskov, T. Bligaard, J. Rossmeisl and C. H. Christensen, *Nat. Chem.*, 2009, **1**, 37–46.

173 G. Kim, Y. Kawazoe and K. R. Lee, *J. Phys. Chem. Lett.*, 2012, **3**, 1989–1996.

174 C. K. Acharya and C. H. Turner, *J. Phys. Chem. B*, 2006, **110**, 17706–17710.

175 C. K. Acharya and C. H. Turner, *J. Phys. Chem. C*, 2007, **111**, 14804–14812.

176 C. K. Acharya, D. I. Sullivan and C. H. Turner, *J. Phys. Chem. C*, 2008, **112**, 13607–13622.

177 G. Ramos-Sanchez and P. B. Balbuena, *Phys. Chem. Chem. Phys.*, 2013, **15**, 11950–11959.

178 S. Kattel and G. F. Wang, *J. Mat. Chem. A*, 2013, **1**, 10790–10797.

179 G. Kim and S. H. Jhi, *ACS Nano*, 2011, **5**, 805–810.

180 Y. Tang, Z. Yang and X. Dai, *J. Nanopart. Res.*, 2012, **14**, 844.

181 M. N. Groves, C. Malardier-Jugroot and M. Jugroot, *J. Phys. Chem. C*, 2012, **116**, 10548–10556.

182 D. Durbin and C. Malardier-Jugroot, *Mol. Simul.*, 2012, **38**, 1061–1071.

183 M. H. Seo, S. M. Choi, E. J. Lim, I. H. Kwon, J. K. Seo, S. H. Noh, W. B. Kim and B. Han, *ChemSusChem*, 2014, **7**, 2609–2620.

184 D. Higgins, M. A. Hoque, M. H. Seo, R. Wang, F. Hassan, J.-Y. Choi, M. Pritzker, A. Yu, J. Zhang and Z. Chen, *Adv. Funct. Mater.*, 2014, **24**, 4325–4336.

185 M. Jain, S. H. Chou and A. Siedle, *J. Phys. Chem. B*, 2006, **110**, 4179–4185.

186 E. Vayner and A. B. Anderson, *J. Phys. Chem. C*, 2007, **111**, 9330–9336.

187 T. S. Olson, S. Pylypenko, S. Kattel, P. Atanassov and B. Kiefer, *J. Phys. Chem. C*, 2010, 15190–15195.

188 Q. He, Q. Li, S. Khene, X. Ren, F. E. Lopez-Suarez, D. Lozano-Castello, A. Bueno-Loopez and G. Wu, *J. Phys. Chem. C*, 2013, **117**, 8697–8707.

189 C. E. Szakacs, M. Lefevre, U. I. Kramm, J.-P. Dodelet and F. Vidala, *Phys. Chem. Chem. Phys.*, 2014, **16**, 13654–13661.

190 S. R. Stoyanova, A. V. Titova and P. Kral, *Coord. Chem. Rev.*, 2009, **253**, 2852–2871.

191 F. Calle-Vallejo, J. I. Martinez and J. Rossmeisl, *Phys. Chem. Chem. Phys.*, 2011, **13**, 15639–15643.

192 S. Kattel, P. Atanassov and B. Kiefer, *J. Phys. Chem. C*, 2012, **116**, 17378–17383.

193 S. Kattel, P. Atanassov and B. Kiefer, *Phys. Chem. Chem. Phys.*, 2014, **16**, 13800–13806.

194 W. Orellana, *J. Phys. Chem. C*, 2013, **117**, 9812–9818.

195 J. Zhang, Z. Wang and Z. Zhu, *J. Power Sources*, 2014, **255**, 65–69.

196 E. F. Holby, G. Wu, P. Zelenay and C. D. Taylor, *J. Phys. Chem. C*, 2014,

118, 14388–14393.
197 J. Sun, Y. H. Fang and Z. P. Liu, *Phys. Chem. Chem. Phys.*, 2014, **16**, 13733–13740.
198 W. Liang, J. Chen, Y. Liu and S. Chen, *ACS Catal.*, 2014, **4**, 4170–4177.
199 A. Klamt and G. Schüürmann, *J. Chem. Soc. Perkin. Trans.*, 1993, **2**, 799–805.
200 D. W. Boukhvalov and Y.-W. Son, *Nanoscale*, 2012, **4**, 417–420.
201 S. F. Huang, K. Terakura, T. Ozaki, T. Ikeda, M. Boero, M. Oshima, J. I. Ozaki and S. Miyata, *Phys. Rev. B.*, 2009, **80**, 235410.
202 Y. Feng, F. Li, Z. Hu, X. Luo, L. Zhang, X.-F. Zhou, H.-T. Wang, J.-J. Xu and E. G. Wang, *Phys. Rev. B*, 2012, **85**, 155454.
203 J. Liang, Y. Jiao, M. Jaroniec and S. Z. Qiao, *Angew. Chemie.*, 2012, 11496–11500.
204 M. Kaukonen, A. V. Krasheninnikov, E. Kauppinen and R. M. Nieminen, *ACS Catalysis*, 2013, **3**, 159–165.
205 B. C. Han, A. V. der Ven, G. Ceder and B.-J. Hwang, *Phys. Rev. B*, 2005, **72**, 205409.
206 B. Han, V. Viswanathan and H. Pitsch, *J. Phys. Chem. C*, 2012, **116**, 6174–6183.
207 L. Zhang, J. Niu, M. Li and Z. Xia, *J. Phys. Chem. C*, 2014, **118**, 3545–3553.
208 Z. Hou, X. Wang, T. Ikeda, K. Terakura, M. Oshima, M.-A. Kakimoto and S. Miyata, *Phys. Rev. B*, 2012, **85**, 165439.
209 L. Zhang, J. Niu, L. Dai and Z. Xia, *Langmuir*, 2012, **28**, 7542–7550.
210 D. Sen, R. Thapa and K. K. Chattopadhyay, *ChemPhysChem*, 2014, **15**, 2542–2549.
211 G. L. Chai, Z. F. Hou, D. J. Shu, T. Ikeda and K. Terakura, *J. Am. Chem. Soc.*, 2014, **136**, 13629–13640.
212 A. J. Stone and D. J. Wales, *Chem. Phys. Lett.*, 1986, **128**, 501–503.
213 Z. F. Hou, D. J. Shu, G. L. Chai, T. Ikeda and K. Terakura, *J. Phys. Chem. C*, 2014, **118**, 19795–19805.
214 D. Kwak, A. Khetan, S. Noh, H. Pitsch and B. Han, *ChemCatChem.*, 2014, **6**, 2662–2670.
215 S. Grimme, *J. Comput. Chem.*, 2006, **27**, 1787–1799.
216 N. Jung, D. Y. Chung, J. Ryu, S. J. Yoo and Y.-E. Sung, *Nano Today*, 2014, **9**, 433–456.
217 Z. Hou, X. Wang, T. Ikeda, S.-F. Huang, K. Terakura, M. Boero, M. Oshima, M. Kakimoto and S. Miyata, *J. Phys. Chem. C*, 2011, **115**, 5392–5403.
218 X. Wang, Z. Hou, T. Ikeda, S.-F. Huang, K. Terakura, M. Boero, M. Oshima, M. Kakimoto and S. Miyata, *Phys. Rev. B*, 2011, 245434.
219 X. Wang, Z. Hou, T. Ikeda, M. Oshima, M. Kakimoto and K. Terakura, *J. Phys. Chem. A*, 2012, **117**, 579–589.
220 K. Artyushkova, B. Kiefer, B. Halevi, A. Knop-Gericke, R. Schlogl and P. Atanassov, *Chem. Commun.*, 2013, **49**, 2539–2541.
221 L. Zhao, R. He, K. T. Rim, T. Schiros, K. S. Kim, H. Zhou, C. Gutierrez, S. P. Chockalingam, C. J. Arguello, L. Palova, D. Nordlund, M. S. Hybertsen, D. R. Reichman, T. F. Heinz, P. Kim, A. Pinczuk, G. W. Flynn and A. N. Pasupathy, *Science*, 2011, **333**, 999–1003.
222 R. A. Sidik, A. B. Anderson, N. P. Subramanian, S. P. Kumaraguru and B. N. Popov, *J. Phys. Chem. B*, 2006, **110**, 1787–1793.
223 K. A. Kurak and A. B. Anderson, *J. Phys. Chem. C*, 2009, **113**, 6730–6734.
224 Y. Okamoto, *App. Surf. Sci.*, 2009, **256**, 335–341.
225 L. Zhang and Z. Xia, *J. Phys. Chem. C*, 2011, **115**, 11170–11176.
226 P. Zhang, X. Hou, J. Mi, Y. He, L. Lin, Q. Jiang and M. Dong, *Phys. Chem. Chem. Phys.*, 2014, **16**, 17479–17486.
227 F. A. Hamprecht, A. J. Cohen, D. J. Tozer and N. C. Handy, *J. Chem. Phys.*, 1998, **109**, 6264.
228 Y. Jiao, Y. Zheng, M. Jaroniec and S. Z. Qiao, *J. Amer. Chem. Soc.*, 2014, **136**, 4394–4403.
229 J. Tomasi, B. Mennucci and R. Cammi, *Chem. Rev.*, 2005, **105**, 2999–3094.
230 A. E. Reed and F. Weinhold, *J. Chem. Phys.*, 1983, **78**, 4066–4073.
231 Y. Zheng, Y. Jiao, L. H. Li, T. Xing, Y. Chen, M. Jaroniec and S. Z. Qiao, *ACS Nano*, 2014, **8**, 5290–5296.
232 S. H. Noh, D. H. Kwak, M. H. Seo and B. H. T. Ohsaka, *Electrochim. Acta*, 2014, **140**, 225–231.
233 M. Sprik and G. J. Ciccotti, *J. Chem. Phys.*, 1998, **109**, 7737–7744.
234 M. Boero, M. Parrinello and K. Terakura, *J. Am. Chem. Soc.*, 1998, **120**, 2746–2752.
235 T. Ikeda, Z. Hou, G.-L. Chai and K. Terakura, *J. Phys. Chem. C*, 2014, **118**, 17616–17625.
236 T. Ikeda, M. Boero, S.-F. Huang, K. Terakura, M. Oshima and J. Ozaki, *J. Phys. Chem. C*, 2008, **112**, 14706–14709.
237 R. Car and M. Parrinello, *Phys. Rev. Lett.*, 1985, **55**, 2471–2474.
238 G. Fazio, L. Ferrighi and C. D. Valentin, *J. Catal.*, 2014, **318**, 203–210.
239 S. Grimme, J. Antony, S. Ehrlich and H. Krieg, *J. Chem. Phys.*, 2010, **132**, 154104.
240 S. Grimme, S. Ehrlich and L. Goerigk, *J. Comput. Chem.*, 2011, **32**, 1456–1465.
241 H. Kim, K. Lee, S. I. Woo and Y. Jung, *Phys. Chem. Chem. Phys.*, 2011, **13**, 17505–17510.
242 H. Jonsson, G. Mills and K. W. Jacobsen, in *Classical and Quantum Dynamics in Condensed Phase Simulations*, ed. B. J. Berne, G. Ciccotti and D. F. Coker, World Scientific, 1998, ch. Nudged Elastic Band Method for Finding Minimum Energy Paths of Transitions, p. 385.
243 E. Gracia-Espino, X. Jia and T. Wågberg, *J. Phys. Chem. C*, 2014, **118**, 2804–2811.
244 J. Liu, Y. Xue, M. Zhang and L. Dai, *MRS Bull.*, 2012, **37**, 1265–1272.
245 M. S. Islam and C. A. J. Fisher, *Chem. Soc. Rev.*, 2013, **43**, 185–204.
246 G. Wang, B. Wang, X. Wang, J. Park, S. Dou, H. Ahn and K. Kim, *J. Mater. Chem.*, 2009, **19**, 8378–8384.
247 X. Fan, W. T. Zheng and J.-L. Kuo, *ACS Appl Mater Interfaces*, 2012, **4**, 2432–2438.
248 M. Khantha, N. Cordero, L. Molina, J. Alonso and L. Girifalco, *Phys. Rev. B*, 2004, **70**, 125422.
249 K. T. Chan, J. B. Neaton and M. L. Cohen, *Phys. Rev. B*, 2008, **77**, 235430.
250 C.-K. Yang, *Appl. Phys. Lett.*, 2009, **94**, 163115.
251 R. E. Mapasha and N. Chetty, *Computational Materials Science*, 2010, **49**, 787–791.
252 P. V. C. Medeiros, F. de Brito Mota, A. J. S. Mascarenhas and C. M. C. de Castilho, *Nanotechnology*, 2010, **21**, 115701.
253 J. Zheng, Z. Ren, P. Guo, L. Fang and J. Fan, *Applied Surface Science*, 2011, **258**, 1651–1655.
254 A. M. Garay-Tapia, A. H. Romero and V. Barone, *J. Chem. Theory Comput.*, 2012, **8**, 1064–1071.
255 L.-J. Zhou, Z. F. Hou and L.-M. Wu, *J. Phys. Chem. C*, 2012, **116**, 21780–21787.
256 J. Song, B. Ouyang and N. V. Medhekar, *ACS Appl Mater Interfaces*, 2013, **5**, 12968–12974.
257 A. Buldum and G. Tetiker, *J. Appl. Phys.*, 2013, **113**, 154312.
258 X. Fan, W. T. Zheng, J.-L. Kuo and D. J. Singh, *ACS Appl Mater Interfaces*, 2013, **5**, 7793–7797.
259 D. Datta, J. Li and V. B. Shenoy, *ACS Appl Mater Interfaces*, 2014, **6**, 1788–1795.
260 E. Lee and K. A. Persson, *Nano Lett.*, 2012, **12**, 4624–4628.
261 Y. Liu, V. I. Artyukhov, M. Liu, A. R. Harutyunyan and B. I. Yakobson, *J. Phys. Chem. Lett.*, 2013, **4**, 1737–1742.
262 E. Pollack, B. Gang, K.-J. Jeon, I. T. Lucas, T. Richadson, F. Wang and R. Kostecki, *Nano Lett.*, 2010, **10**, 3386–3388.
263 L.-J. Zhou, Z. F. Hou, L.-M. Wu and Y.-F. Zhang, *J. Phys. Chem. C*, 2014, **118**, 28055–28062.

264 C. Uthaisar and V. Barone, *Nano Lett.*, 2010, **10**, 2838–2842.
265 X. Li, Y. Hu, J. Liu, A. Lushington, R. Li and X. Sun, *Nanoscale*, 2013, **5**, 12607.
266 E. M. Lotfabad, J. Ding, K. Cui, A. Kohandehghan, W. P. Kalisvaart, M. Hazelton and D. Mitlin, *ACS Nano*, 2014, **8**, 7115–7129.
267 C. Ma, X. Shao and D. Cao, *J. Mater. Chem.*, 2012, **22**, 8911–8915.
268 X.-k. Kong and Q.-w. Chen, *Phys. Chem. Chem. Phys.*, 2013, **15**, 12982–12987.
269 R. Lu, D. Rao, Z. Meng, X. Zhang, G. Xu, Y. Liu, E. Kan, C. Xiao and K. Deng, *Phys. Chem. Chem. Phys.*, 2013, **15**, 16120–16126.
270 C. Ling and F. Mizuno, *Phys. Chem. Chem. Phys.*, 2014, **16**, 10419–10424.
271 D. Das, S. Kim, K.-R. Lee and A. K. Singh, *Phys. Chem. Chem. Phys.*, 2013, **15**, 15128–15134.
272 R. P. Hardikar, D. Das, S. S. Han, K.-R. Lee and A. K. Singh, *Phys. Chem. Chem. Phys.*, 2014, **16**, 16502–16508.
273 A. L. M. Reddy, A. Srivastava, S. R. Gowda, H. Gullapalli, M. Dubey and P. M. Ajayan, *ACS Nano*, 2010, **4**, 6337–6342.
274 Z.-S. Wu, W. Ren, L. Xu, F. Li and H.-M. Cheng, *ACS Nano*, 2011, **5**, 5463–5471.
275 H. Zhang, M. Zhao, X. He, Z. Wang, X. Zhang and X. Liu, *J. Phys. Chem. C*, 2011, **115**, 8845–8850.
276 K. Srinivasu and S. K. Ghosh, *J. Phys. Chem. C*, 2012, **116**, 5951–5956.
277 H. Zhang, Y. Xia, H. Bu, X. Wang, M. Zhang, Y. Luo and M. Zhao, *J. Appl. Phys.*, 2013, **113**, 044309.
278 S. Grimme, S. Ehrlich and L. Goerigk, *J. Comp. Chem.*, 2011, **32**, 1456–1465.